MEMORY FORMATION

Diversity in neural firing dynamics supports both rigid and learned hippocampal sequences

Andres D. Grosmark[1,2] and György Buzsáki[2,3]*

Cell assembly sequences during learning are "replayed" during hippocampal ripples and contribute to the consolidation of episodic memories. However, neuronal sequences may also reflect preexisting dynamics. We report that sequences of place-cell firing in a novel environment are formed from a combination of the contributions of a rigid, predominantly fast-firing subset of pyramidal neurons with low spatial specificity and limited change across sleep-experience-sleep and a slow-firing plastic subset. Slow-firing cells, rather than fast-firing cells, gained high place specificity during exploration, elevated their association with ripples, and showed increased bursting and temporal coactivation during postexperience sleep. Thus, slow- and fast-firing neurons, although forming a continuous distribution, have different coding and plastic properties.

The restructuring of hippocampal networks through synaptic plasticity is necessary for the formation of new episodic memories. Replay of hippocampal place-cell (*1*) sequences during sharp wave ripples (SPW-Rs) of waking immobility (*2*–*5*) and non–rapid eye movement sleep (*6*–*13*) after learning has been proposed to support memory consolidation (*10*–*13*). Replay is conceptualized and typically studied as a phenomenon with higher-order interactions within populations of neurons taken to have similar properties (*10*, *14*). However, networks built from similar neurons are unstable (*15*), and recent findings demonstrate that biophysical properties of cortical pyramidal neurons are highly diverse and characterized by lognormal distributions of synaptic weights, long-term firing rates, and spike bursts (*16*). Furthermore, temporal correlations of hippocampal neurons are largely preserved across brain states and environmental situations, suggesting that learning-induced changes are constrained within a dynamically stable network (*16*, *17*). An example of a preexisting bias between place-cell sequences in a novel environment and sleep before the novel experience (preplay) has been described (*18*–*20*), although its computational relevance has been questioned recently (*14*). To clarify the relationship between preexisting biophysical properties of neurons and their contribution to learning, characterization of individual neurons is necessary. We performed such analyses during sleep in rats before and after they explored a novel environment.

Simultaneous recordings of well-isolated CA1 pyramidal single units were performed in four rats. Several methods were used to assess the relationship between firing patterns during exploration of one of two linear or a circular track (MAZE) in rooms B, C and D, respectively, and candidate SPW-R sequences during preexperience sleep (PRE) and postexperience sleep (POST) in the home cage in room A (fig. S1) (*21*). First, a spatial Bayesian decoder (*2*), constructed from the firing-rate vectors of place cells (n = 491 cells) during track running (eight novel exploration sessions), was applied to all candidate ripple events (*21*) (figs. S2 to S4) of PRE, MAZE, and POST immobility epochs to estimate the posterior probabilities of position in forward (*2*, *5*, *9*) or reverse virtual traversals of the track (*3*, *4*) (Fig. 1, A and B). These virtual traversals were measured as weighted correlations over the Bayesian derived posteriors for place across all 20-ms bins in each ripple event (*21*) and normalized as Z scores [*rZ* (sequence score) (*21*)] (figs. S5 to S8).

To determine each place cell's contribution to PRE and POST sequences [per cell contribution (PCC)], a PCC score was defined as the neuron's mean contribution across all PRE and POST putative events as determined by a cell-specific shuffling technique (*21*). Neurons that showed significant PCC scores in either PRE or POST were considered to be strongly contributing to sequence formation (n = 216 neurons (Fig. 2B) (*21*). Importantly, the majority of neurons strongly contributing to PRE (73%) also contributed to POST sequences (Fig. 2C and fig. S19), suggesting that these neurons represent rigid network elements. Strongly contributing neurons < 50 percentile of that session's PRE to POST sleep PCC change (ΔPCC) were classified as rigid cells (blue x's in Fig. 2B), whereas those > 50 percentile as plastic cells (red x's in Fig. 2A and figs. S9 to 11). Rigid and plastic neurons were similarly distributed along the track (fig. S2). The contribution of individual neurons to the overall population ΔPOST-PRE score (POST *rZ* – PRE *rZ*) was assessed by either shuffling or excluding neurons with increasing or decreasing ΔPCC scores from the analysis (Fig. 2C and fig. S12) (*21*). Replay (POST > PRE) was eliminated after shuffling or removal of the top 10 to 20% of cells with the highest ΔPCC scores, whereas it remained after shuffling or removal of the bottom 75% (Figs. 2, C and D, and fig. S12). These results suggest that from the PRE to the POST sleep, plastic neurons are added to a preexisting backbone structure, leading to an increase in maze-related sequential activity (replay) associated with learning (Fig. 2C)

Although both rigid and plastic neurons contributed to replay sequences, the nature of their representation was different. Plastic neurons had higher place-specific indices and fewer place fields compared with rigid cells (Fig. 3A), and plastic but not rigid neurons increased their spatial specificity steadily during learning (Fig. 3B and fig. S13). Neither overall firing-rate changes (figs. S14 and S15) nor potential errors in neuronal clustering or neuron classification (figs. S2 and S11) could account for the above differences. These findings suggest that precision in spatial coding is a property developed during maze running by a small plastic subset of cells.

Next, we asked whether rigid and plastic neurons have different biophysical and network properties. Session-wide firing rates of rigid neurons were significantly higher compared with plastic neurons (Fig. 4, A and B, and figs. S14 and S15). Ripple-related spiking, bursting, and pair-wise coactivation were higher in plastic versus rigid neurons (Fig. 4A and figs. S14 to S16). In PRE sleep, coactivity was dominated by fast-firing neurons, and these correlations remained unchanged into POST sleep. In contrast, slow-firing neurons showed the strongest increases in coactivation from PRE to POST sleep (Fig. 4B). Pair-wise coactivity and temporal bias patterns were stable from PRE to POST for pairs of rigid cells, whereas plastic cell pair interactions were modified by experience on the novel maze (*10*) (figs. S16 and S17).

Because the above analyses indicated that overall firing rates and ripple-related activity of neurons predicted their coding and plastic features, in our final analysis we divided place cells into equal subgroups by either "off-line" sleep-firing rate or ripple-rate gain and repeated the Bayesian place decoding analysis for each group. Low-rate neurons (median, 0.39 Hz) contributed more spatial information per spike on the maze and displayed increased within-ripple firing-rate gains from PRE to POST sleep than high-rate cells (median, 1.12 Hz) (fig. S16). Slow-firing, but not fast-firing, neurons increased their contribution to neuronal sequences from PRE to POST sleep (Fig. 4D). Conversely, PRE to POST increases in sequence content were limited to cells that showed a high degree of ripple-specific recruitment (gain) (Fig. 4E and figs. S20 to S22), suggesting that ripples are privileged windows for learning-related changes in excitability. Similar results were obtained using several Bayesian and non-Bayesian replay methods (figs. S19 to S22).

Using several established and newly developed methods, we demonstrate that sequences of place cells in a novel environment are formed from a combination of relatively fast-firing group of pyramidal neurons with relatively unchanging temporal dynamics and a slow-firing plastic subset of

[1]Department of Neuroscience, Columbia University Medical Center, New York, NY 10019, USA. [2]The Neuroscience Institute, School of Medicine, New York University, New York, NY 10016, USA. [3]Center for Neural Science, New York University, New York, NY 10016, USA.
*Corresponding author. E-mail: gyorgy.buzsaki@nyumc.org

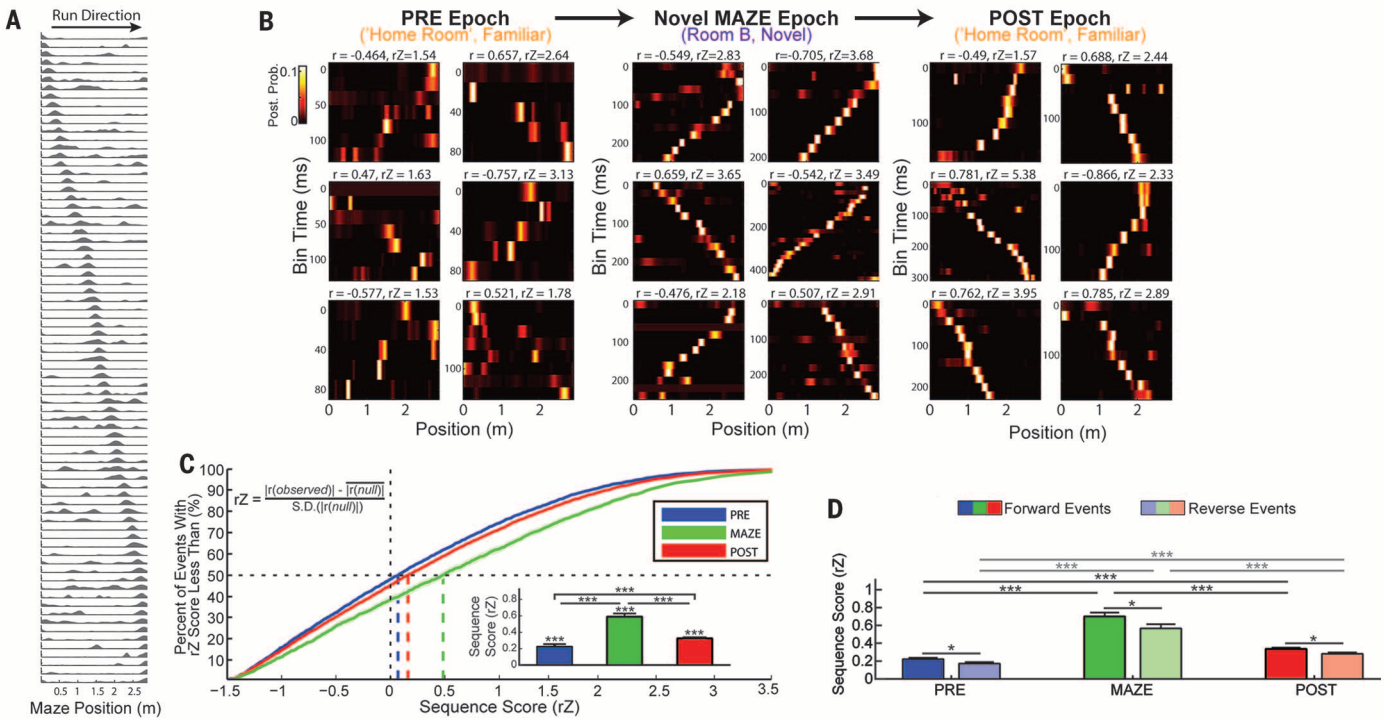

Fig. 1. PRE and POST maze sequence events. (**A**) Simultaneous recording of 77 place cells (rightward runs) used to generate a sequence template. (**B**) Representative forward and reverse sequences during PRE maze sleep, immobility in the novel MAZE, and POST-learning sleep. (**C**) Cumulative distribution of *rZ* for PRE, MAZE, and POST events, and 95% confidence intervals. Vertical dashed lines, medians. Inset, mean ± SE of sequence scores in each condition. $*P < 0.05$; $**P < 0.005$; $***P < 0.0005$ (Kruskal-Wallis test, followed by post hoc Tukey-Kramer tests). Sign-rank tests were used for within-condition significance testing. (**D**) As inset in (C), but events with forward and reverse sequences are shown separately (within epoch comparisons, ranked-sum test).

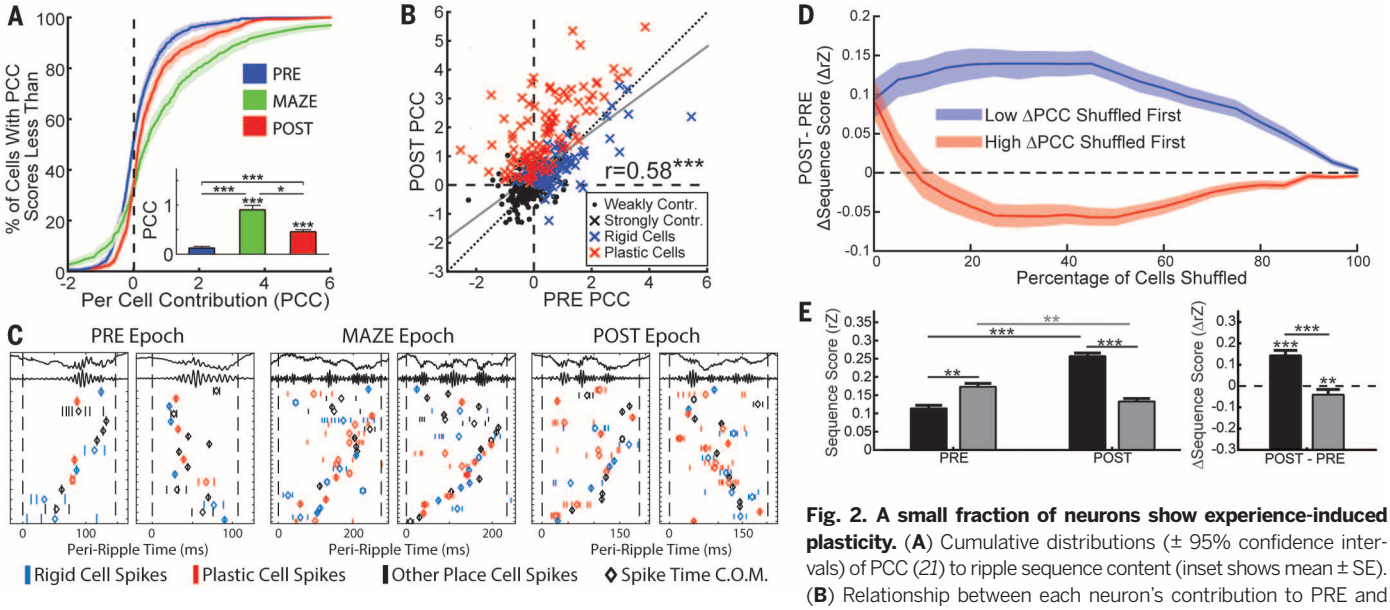

Fig. 2. A small fraction of neurons show experience-induced plasticity. (**A**) Cumulative distributions (± 95% confidence intervals) of PCC (*21*) to ripple sequence content (inset shows mean ± SE). (**B**) Relationship between each neuron's contribution to PRE and POST sequence content. Gray line, least-squared regression between all PRE and POST PCC scores. Neurons strongly contributing to either PRE or POST (*21*) are marked with X; others are marked with dots. Strongly contributing neurons in the lower 50th percentile of that session's PRE versus POST change (ΔPCC) were considered rigid cells and those in the upper 50th percentile as plastic cells. (**C**) Raster and local field potential (LFP) plots of example ripple events from the PRE, MAZE, and POST epochs (diamonds show within-ripple spike-time center of mass). These six events correspond to the top row of Fig. 1B. Rigid and plastic cell spikes are shown in blue and red, respectively. Although rigid cells tend to predominate in the PRE epoch, the marked increase in sequence content observed in the MAZE and POST epochs is driven by the recruitment of plastic cells. (**D**) To assess the contribution of neurons with differing ΔPCC scores to the change in virtual travel content from the PRE to the POST epoch, the replay analysis was repeated using templates in which an increasing percentage (*x* axis) of neuron's place fields were shuffled either beginning with those that showed the lowest ΔPCC values (blue line) (shaded area shows bootstrapped 95% confidence interval) or beginning with neurons with the highest ΔPCC scores (red line). (**E**) Effect on sequence content of removal of rigid (black) or plastic (gray) neurons. The PRE to POST increase in sequence content is attributable to only a small number of plastic cells.

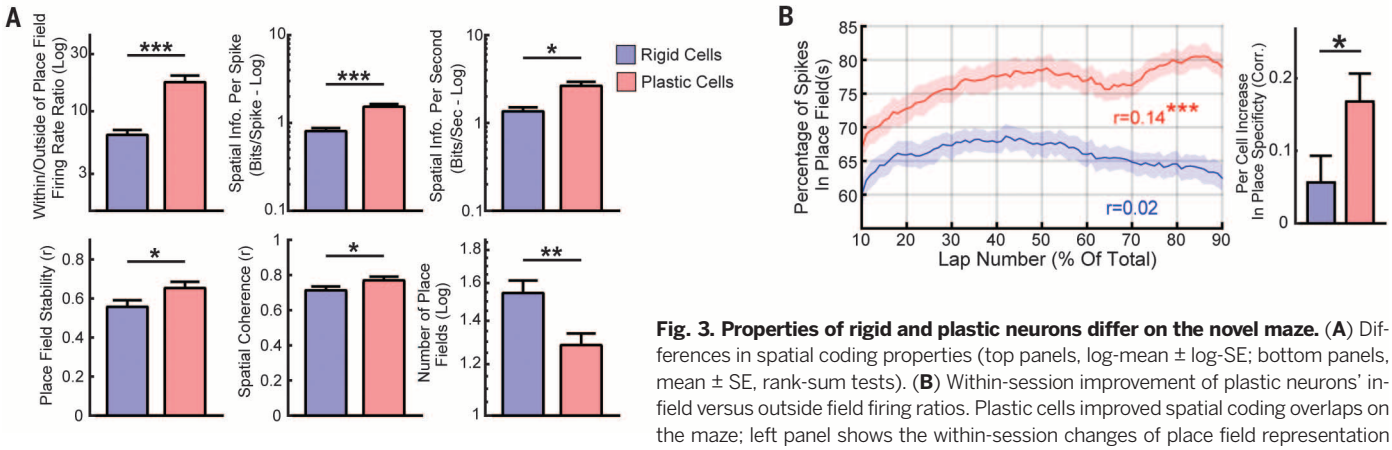

Fig. 3. Properties of rigid and plastic neurons differ on the novel maze. (**A**) Differences in spatial coding properties (top panels, log-mean ± log-SE; bottom panels, mean ± SE, rank-sum tests). (**B**) Within-session improvement of plastic neurons' in-field versus outside field firing ratios. Plastic cells improved spatial coding overlaps on the maze; left panel shows the within-session changes of place field representation for rigid (blue) or plastic (red) neurons (shaded region shows bootstrapped 95% confidence interval). Right panel, per cell summary of within-field firing specificity changes (mean ± SE) (*21*).

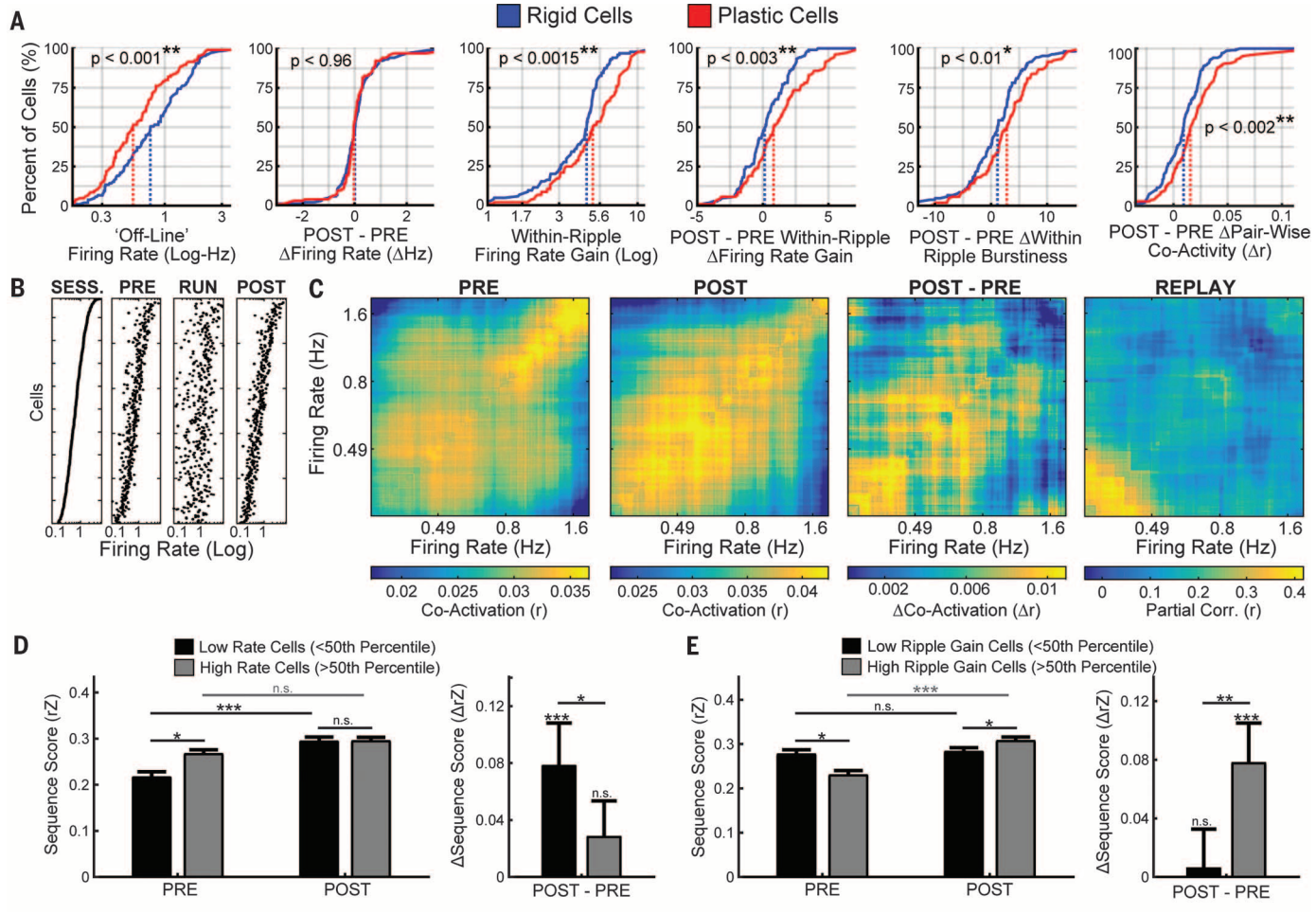

Fig. 4. Low-firing-rate, high-ripple-recruitment neurons show high learning-related plasticity. (**A**) Summary of excitability and synchrony profiles of rigid and plastic cells. Each panel shows the cumulative distributions of the two groups; dashed lines show medians (*P* values, rank-sum tests). (**B**) To examine the relationship between firing rates and learning-related changes in pair-wise coactivation (Pearson's correlation of firing rates in 100-ms bins), neurons in PRE, MAZE, and POST were sorted by their overall session (SESS) firing rates [(B), left panel]. (**C**) Coactivation was assessed across overlapping groups each containing 20% of place cells with similar firing rates (step size, 1% of cells). Although fast-firing cells dominated the coactivation structure during the PRE (left panel), it was the slow-firing cells that showed the highest increase in coactivation from PRE to POST (middle two panels). Moreover, it was the slow-firing cells that showed the greatest replay (partial correlation across coactivation values between RUN and POST, accounting for PRE). (**D** and **E**) An additional replay analysis restricted to place cells with either low or high firing rates (D) or within-ripple firing-rate gains [(E), annotation same as in Fig. 2D] confirms the findings obtained using the PCC method.

neurons (*22*). Firing properties of neurons predicted their rigid (*18*, *19*) and plastic (*10*) features. Slow-firing neurons gained high place specificity during maze exploration (*23*, *24*) and showed increased ripple-related recruitment during POST-experience sleep. In contrast, fast-firing neurons had low selectivity (*16*, *25*), have been shown previously to project to multiple targets (*26*) and to form an interactive subnetwork responsible for global stability, thus allowing plasticity to take place in the remaining majority of slow-firing cells (*16*, *17*). Fast-firing neurons may generalize across situations, whereas slow-firing neurons may differentiate among them (*27*). Because replay sequence-forming neurons are drawn from the wide span of a continuous log-rate distribution (*16*) with varying coding, biophysical, circuit, and plasticity properties, these events can forward a synthesis of preexisting and new information to downstream observer neurons.

REFERENCES AND NOTES

1. J. O'Keefe, L. Nadel, *The Hippocampus as a Cognitive Map* (Oxford Univ. Press, 1978).
2. T. J. Davidson, F. Kloosterman, M. A. Wilson, *Neuron* **63**, 497–507 (2009).
3. K. Diba, G. Buzsáki, *Nat. Neurosci.* **10**, 1241–1242 (2007).
4. D. J. Foster, M. A. Wilson, *Nature* **440**, 680–683 (2006).
5. B. E. Pfeiffer, D. J. Foster, *Nature* **497**, 74–79 (2013).
6. D. Dupret, J. O'Neill, B. Pleydell-Bouverie, J. Csicsvari, *Nat. Neurosci.* **13**, 995–1002 (2010).
7. G. Girardeau, K. Benchenane, S. I. Wiener, G. Buzsáki, M. B. Zugaro, *Nat. Neurosci.* **12**, 1222–1223 (2009).
8. H. S. Kudrimoti, C. A. Barnes, B. L. McNaughton, *J. Neurosci.* **19**, 4090–4101 (1999).
9. A. K. Lee, M. A. Wilson, *Neuron* **36**, 1183–1194 (2002).
10. M. A. Wilson, B. L. McNaughton, *Science* **265**, 676–679 (1994).
11. G. Buzsáki, *Neuroscience* **31**, 551–570 (1989).
12. M. E. Hasselmo, *Trends Cogn. Sci.* **3**, 351–359 (1999).
13. G. Buzsáki, *Hippocampus* **25**, 1073–1188 (2015).
14. D. Silva, T. Feng, D. J. Foster, *Nat. Neurosci.* **18**, 1772–1779 (2015).
15. W. Gerstner, W. M. Kistler, R. Naud, L. Paninski, *Neuronal Dynamics: From Single Neurons to Networks and Models of Cognition* (Cambridge Univ. Press, 2014).
16. K. Mizuseki, G. Buzsáki, *Cell Rep.* **4**, 1010–1021 (2013).
17. D. Panas *et al.*, *J. Neurosci.* **35**, 8480–8492 (2015).
18. G. Dragoi, S. Tonegawa, *Nature* **469**, 397–401 (2011).
19. G. Dragoi, S. Tonegawa, *Proc. Natl. Acad. Sci. U.S.A.* **110**, 9100–9105 (2013).
20. H. F. Ólafsdóttir, C. Barry, A. B. Saleem, D. Hassabis, H. J. Spiers, *eLife* **4**, e06063 (2015).
21. Materials and methods are available as supplementary materials on *Science* Online.
22. G. Dragoi, K. D. Harris, G. Buzsáki, *Neuron* **39**, 843–853 (2003).
23. K. C. Bittner *et al.*, *Nat. Neurosci.* **18**, 1133–1142 (2015).
24. S. Cheng, L. M. Frank, *Neuron* **57**, 303–313 (2008).
25. P. D. Rich, H.-P. Liaw, A. K. Lee, *Science* **345**, 814–817 (2014).
26. S. Ciocchi, J. Passecker, H. Malagon-Vina, N. Mikus, T. Klausberger, *Science* **348**, 560–563 (2015).
27. G. Buzsáki, *Science* **347**, 612–613 (2015).

ACKNOWLEDGMENTS

This work was supported by NIH grants NS075015, MH54671, and MH102840; the Simons Foundation; and the G. Harold and Leila Y. Mathers Foundation. We thank J. Long for invaluable experimental support and B. Watson, S. McKenzie, L. Roux, and S. Tuncdemir for discussion and advice. Spike and LFP data are available at CRCNS.org.

SUPPLEMENTARY MATERIALS

www.sciencemag.org/content/351/6280/1440/suppl/DC1
Materials and Methods
Figs. S1 to S22
References (*28*–*36*)

6 August 2015; accepted 11 February 2016
10.1126/science.aad1935

NEURODEVELOPMENT

Sequential transcriptional waves direct the differentiation of newborn neurons in the mouse neocortex

Ludovic Telley,[1,7]* Subashika Govindan,[1,7]* Julien Prados,[1,7] Isabelle Stevant,[2,7] Serge Nef,[2,7] Emmanouil Dermitzakis,[2,5,6,7] Alexandre Dayer,[1,3,7] Denis Jabaudon[1,4,7]†

During corticogenesis, excitatory neurons are born from progenitors located in the ventricular zone (VZ), from where they migrate to assemble into circuits. How neuronal identity is dynamically specified upon progenitor division is unknown. Here, we study this process using a high-temporal-resolution technology allowing fluorescent tagging of isochronic cohorts of newborn VZ cells. By combining this in vivo approach with single-cell transcriptomics in mice, we identify and functionally characterize neuron-specific primordial transcriptional programs as they dynamically unfold. Our results reveal early transcriptional waves that instruct the sequence and pace of neuronal differentiation events, guiding newborn neurons toward their final fate, and contribute to a road map for the reverse engineering of specific classes of cortical neurons from undifferentiated cells.

During neocortical development, distinct classes of neurons assemble to form local and long-range circuits. Although class-specific genes and features identify cortical neuron types relatively late in differentiation (*1*–*5*), early postmitotic fate specification programs have been inaccessible. Here, we describe the dynamic transcriptional activity controlling layer 4 (L4) excitatory neuron birth and differentiation in the mouse neocortex.

Mammalian cortical progenitor cells in the ventricular zone (VZ) undergo DNA synthesis [S-phase, susceptible to bromodeoxyuridine (BrdU) labeling] at the basal border of the VZ and mitosis (M-phase, lasting about an hour at midcorticogenesis in mice) when their soma is apically located, adjacent to the ventricular space (*6*, *7*). At this location, mitotic cells are susceptible to labeling by intraventricular injection of carboxyfluorescein esters ["FlashTag" (FT)], which bind to and fluorescently label intracellular proteins (*8*). The short extracellular half-life of FT in the mouse ventricular space ensures effective pulse-labeling of juxtaventricular dividing cells (Fig. 1A and fig. S1). Intracellularly, FT is linearly diluted at each mitosis, such that fluorescence reflects the number of cell divisions that have occurred since the time of labeling (fig. S1, D and E, and movie S1) (*8*). FT$^+$ newborn cells synchronously moved away from the ventricular wall within 3 hours of labeling (Fig. 1A, bottom), reached the subventricular zone (SVZ) within 12 hours, and entered the cortical plate (CP) 24 to 48 hours after mitosis (Fig. 1B). Isochronic cohorts of VZ cells born at the time of injection can thus be specifically identified and tracked during their initial differentiation.

The laminar fate of FT$^+$ neurons was linked to the day of FT injection at all ages examined [embryonic day (E) 11.5 to 17.5] (fig. S2 and Fig. 1C). At postnatal day (P) 7, when neuronal migration is complete, E14.5-labeled FT$^+$ neurons were restricted to a sublamina of L4 (Fig. 1C). These neurons were born at the time of the FT pulse, not later, because they mostly remained unlabeled after continuous BrdU administration beginning at the time of the FT pulse (fig. S1, B to D). Injection of FT at E14 and E14.5 using two dye colors in the same embryo showed two distinct populations of labeled neurons within L4 at P7, revealing a tight relationship between time of birth and final radial location, even within a single layer (Fig. 1D). Thus, we used E14.5 FT injections to label L4 neurons in vivo from the time of mitosis in the VZ and track their early molecular differentiation.

We observed that newborn cells sequentially expressed PAX6, a VZ marker, TBR2 a SVZ marker, and the early neuronal protein TBR1 (*9*, *10*) within the first 48 hours after mitosis (fig. S3). This reveals a highly dynamic cellular process characterized by overlapping signature shifts in protein expression. For an unbiased account of the transcriptional programs active just after cell birth in single cells, we isolated E14.5-born FT$^+$ cells 6, 12, 24, and 48 hours after mitosis by using cortical microdissection followed by fluorescence-activated cell sorting

[1]Department of Basic Neurosciences, University of Geneva, Switzerland. [2]Department of Genetic Medicine and Development, University of Geneva, Switzerland. [3]Department of Psychiatry, Geneva University Hospital, Switzerland. [4]Clinic of Neurology, Geneva University Hospital, Switzerland. [5]Biomedical Research Foundation Academy of Athens, Greece. [6]Center of Excellence in Genomic Medicine Research, King Abdulaziz University, Saudi Arabia. [7]Institute for Genetics and Genomics in Geneva (iGE3), University of Geneva, Switzerland.
*These authors contributed equally to this work. **†Corresponding author. E-mail: denis.jabaudon@unige.ch**

Editor's Summary

Coding what is known and what is new

Do neural activity patterns during sleep reflect the replay of a novel experience or an invariant preexisting dynamic? Grosmark and Buzsáki observed that both familiar and novel aspects of learned information are replayed during synchronous bursts of activity in the hippocampus. Familiarity was encoded by fast-firing less-modifiable neurons that showed rate and sequence correlations that persisted into postlearning sleep. The novel features of an experience were represented by a different set of slowly firing and highly plastic cells.

Science, this issue p. 1440

www.sciencemag.org/content/351/6280/1440/suppl/DC1

Supplementary Materials for

Diversity in neural firing dynamics supports both rigid and learned hippocampal sequences

Andres D. Grosmark and György Buzsáki*

*Corresponding author. E-mail: gyorgy.buzsaki@nyumc.org

Published 25 March 2016, *Science* **351**, 1440 (2016)
DOI: 10.1126/science.aad1935

This PDF file includes:

Materials and Methods

Animals, Surgery and Data Collection

Four male Long-Evans rats (250-350g) were bilaterally implanted in the dorsal hippocampus with either two 8 shank (n = 2; BUZ64) or two 6 shank (n = 2; BUZ64SP) silicon probes. Each shank of the 8-shank silicon probes had 8 sites while each shank of the 6-shank silicon probes had 10 sites. All sites were vertically staggered along the shank with 20 μm spacing between sites. Each site had an area of 160 μm^2 and an impedance of 1–3 MΩ. In each rat, 50 μm wires were placed gently abutting the left, right mastoid masseter as well as the back neck muscle for electromyographic (EMG) recordings used in sleep classification. All silicon probes were implanted parallel to the septo-temporal axis of the dorsal hippocampus. Finally, each rat was fitted with a small 3-dimensional accelerometer to record the animals' movement, or its absence, during sleep. Two stainless steel screws implanted above the cerebellum were used for referencing and grounding. Implantation was performed under isoflurane (1-1.5%) anesthesia as previously described (*28*). Each silicon probe was attached to a micromanipulator and lowered over the course of several days until hippocampal layer CA1 was reached as determined by the appearance of hippocampal CA1 sharp wave-ripple s and pyramidal cell activity. Probe placement was histologically confirmed *post hoc*.

Animals were extensively handled both before and after surgery. Water restriction was initiated one week after the surgery; animals were restricted to 90% of their initial body weight and given one day a week of *ad lib* water access. Animals were well acclimatized and recorded in the 'familiar' room (where all sleep recordings were performed) for at least one week prior to novelty maze sessions. This time was used to gradually lower the silicon probes into position. All hippocampal, EMG and accelerometer signals were recorded continuously at 20 kHz using four identical 256-channel Amplipex Systems (16-bit resolution; analog multiplexing; one in the familiar room and one in each of the two novelty rooms). Extracellular cell clustering and classification was performed as has been previously described (*29*). In total, 562 well isolated pyramidal cells were included in this study. All protocols were approved by the Institutional Animal Care and Use Committee of New York University.

Behavioral Procedures and Behavioral State Scoring

To acclimatize the rats to running for reward, rats were pre-trained to search for water on a geometrically unrelated open-field 'cheese-board' maze (*30*) for several days before novelty maze sessions. Once electrodes reached the CA1 pyramidal layer and the

animals were well acclimatized to running for water reward as well as to the 'familiar' room as determined by the observation that the animals engaged in uninterrupted sleep in this room, a 'novelty' session was recorded. A novelty session consisted of a 'PRE' epoch in the familiar room, a novelty run in one of the three novel rooms and 'POST' epoch back in the familiar room. Only one novelty room was used per novelty session. Note also that in recent studies (*14, 18, 19*) novelty to the context of the experimental room was established by occluding the experimental room by placing walls around the home cage during 'PRE' and 'POST' epochs. In contrast, in the present study the animals had never been inside of the novel rooms, ensuring that the animals had no experience of the maze context, even fleeting ones during the plugging of the electrophysiological headstages, prior to novelty exposure.

On novelty days the animals were recorded in their home cage in the familiar room and allowed to sleep for approximately four hours, constituting the PRE novelty epoch. At the end of the PRE epoch, the animals were transferred to one of three novelty rooms, housing a 1.9 m wooden linear maze (n = 4 sessions), or a 2.3 m metal linear maze (n = 1 session), or a 1 m in diameter wooden circular maze (n = 3 sessions). The linear mazes consisted of 15 cm 'reward areas' on either end where water reward was delivered via an automatic infrared-beam triggered system, and a 1.6 m, or 2 m 'stem'. Rats only received water reward (~0.2 ml) for trials in which they travelled from one reward site to the other. On the circular maze rats were made to run in a clockwise direction by preventing the counter-clockwise movement until the rats' behavior became stereotyped (~10 minutes). Water reward (~0.2 ml) was delivered in a predetermined 30 cm reward area only when the animals had performed a full clockwise run. The RUN sessions were terminated once the animals were satiated and no longer ran for reward. In both the circular and the linear mazes the animal's position was monitored by the continuous tracking at 39.69 Hz of two LEDs (red and blue) positioned 5 cm apart and clipped onto the animal's headmounted Faraday cage. Subsequent to novelty exposure, the animal was transferred back to its homecage in the familiar room and allowed to sleep for approximately four hours, constituting the POST epoch. All sleep and novelty recordings were performed during the animal's day-cycle when rats are prone to sleep.

Sleep scoring was performed using hippocampal LFP (theta/delta ratio), accelerometer (movement), and E.M.G. data as previously described (*31*). For each session all PRE and POST epoch analysis was yoked to the duration of the shortest of the two epochs of each session.

Place Field Analysis

For each well isolated principal cell a spike firing-by-position vector was constructed by binning its spikes in non-overlapping 2 cm bins. This vector was smoothed with a 5 cm Gaussian kernel, and divided by the smoothed (5 cm Gaussian kernel) occupancy-by-position resulting in a smoothed position by-firing rate vector. In the case of the circular maze location was linearized and defined as starting at the edge of reward area, and increasing clockwise, terminating at the opposing edge of the reward area. The hypothesis of place-selective firing was tested by constructing 5,000 null firing rate vectors in which the cell's spikes were randomly sampled using the un-smoothed occupancy-by-position vector as the probability density function, smoothed with a 5cm Gaussian kernel and divided by the smoothed occupancy-by-position vector. A cell was determined to have a place field (and thus, to be a place cell) if at least 5 consecutive bins were above the 99^{th} percentile of their null distributions and the cell exhibited a within-field peak firing rate of at least 1Hz. All place field detection analysis was restricted to epochs during which the animal's velocity was at least 5 cm/s and in which the rat was outside of the reward areas. For linear track maze runs all place field analysis was carried out independently for left and right directions of movement (*3*, *4*, *18*). Standard measures of place field properties (information per spike, information per second, spatial coherence and stability) were performed in the same manner as in (*32*)).

Ripple Event Detection

Ripple events were conditioned on the coincidence of both population synchrony events, and LFP detected ripples. For each session the combined spiking of all recorded CA1 pyramidal cells were binned in 1ms bins and convolved with a 15 ms Gaussian kernel (*5*). For each session a trigger rate was defined as being 3 standard deviations above the mean of all 1 ms bins within NREM epochs of both PRE and POST epochs combined. Putative population synchrony events were detected when the smoothed firing rate vector crossed the trigger rate. The beginning and end of the putative synchrony events were defined as the time points at which the convolved firing rate vector returned to the mean of all within-NREM firing rate bins. Independently, sharp wave-ripple events were detected from the pyramidal layer LFP. Population synchrony events that did not contain at least one LFP-detected ripple (as assessed by the time-stamp of its peak ripple power) were discarded (50.6% of population events met this criteria). Population synchrony events which 1) contained at least one LFP-detected sharp wave-ripple, 2) lasted between 50 to 500 ms, and 3) occurred during non-theta or 'off-line' states (quite waking [immobility] or NREM) and 4) in which at least five distinct pyramidal cells each fired at least one spike were termed '*Ripple events'* and considered for further analysis. This five pyramidal cell inclusion criteria was used as it is the minimum number of cells

needed to establish significance for sequence relationship between cells at $p < 0.05$ (5! = 120 possible orderings, of which half are mirror 'forward' and 'reverse' sequences and hence equivalent with respect to the sequence analysis, resulting in 60 unique orderings, 1/60 = 0.0167).

Bayesian Replay Analysis

For linear track sessions Bayesian analysis was performed independently for the left and right direction of movement. Only ripple events with durations of at least 100 ms and in which at least 10% or 5 (whichever was greater) of place cells fired were considered for this analysis – note that these criteria were applied consistently including in analysis where certain sub-groups of cells were excluded. These ripple events were subdivided into non-overlapping 20 ms bins, and firing rate vectors for all place cells were constructed within these bins. For each of these binned firing rate vectors, smooth-prior probability, Bayesian classification of virtual position (*2*) was performed utilizing a template comprising of all place cell's smoothed firing rate-by-position vectors as:

$$Pr(pos \mid spikes) = \left(\prod_{i=1}^{n} f_i(pos)^{sp_i}\right) e^{-\tau \sum_{i=1}^{n} f_i(pos)} \quad (1)$$

Where $f_i(pos)$ is the value of the firing rate-by-position vector of the i^{th} place cell at position *pos*, sp^i is the number of spikes fired by the i^{th} place cell in the time bin being decoded, τ is the duration of the time bin (0.02 seconds) and n is the total number of place cells. Posterior probabilities were subsequently normalized to one:

$$Pr(pos \mid spikes) = \frac{Pr(pos \mid spikes)}{\sum_{i=1}^{P_n} Pr(pos_i \mid spikes)} \quad (2)$$

Where P_n is the total number of positions (2 cm bins).

For each decoded ripple event a measure of Bayesian *Reconstruction Quality* was derived as the median across within-ripple-event 20 ms time-bins of the maximal posterior probability value for each time bin.

Subsequently a preliminary sequence score (r) was computed for each event as the correlation of time and position, as weighted by posterior probability ($r(pos, bin; Pr)$(*33*). For a given event the weighted mean m is given by:

$$m(pos; Pr) = \sum_{i=1}^{M} \sum_{j=1}^{N} Pr_{ij} pos_j \Big/ \sum_{i=1}^{M} \sum_{j=1}^{N} Pr_{ij} \quad (3)$$

The weighted covariance *cov*:

$$\mathrm{cov}(pos, bin; Pr) = \frac{\sum_{i=1}^{M}\sum_{j=1}^{N} Pr_{ij}\left(pos_j - \mathrm{m}(pos; Pr)\right)\left(bin_i - \mathrm{m}(bin; Pr)\right)}{\sum_{i=1}^{M}\sum_{j=1}^{N} Pr_{ij}} \quad (4)$$

And the weighted correlation *r(pos, bin; Pr):*

$$r(pos, bin; Pr) = \frac{\mathrm{cov}(pos, bin; Pr)}{\sqrt{\mathrm{cov}(pos, pos; Pr)(\mathrm{cov}(bin, bin; Pr)}} \quad (5)$$

Where pos_j is the j^{th} spatial bin, bin_i is the i^{th} temporal (20 ms) bin in the event, Pr_{ij} is the Bayesian posterior probability for that spatial bin at that temporal bin, *M* is the total number of temporal bins and *N* is the total number of spatial bins.

For Forward and Reverse replay analyses (Fig. 1C and fig. S7C), a separate Bayesian decoder was applied to ripple events in each direction in the bi-directional linear mazes. The 'template' for the directionality decoder was taken as the firing rate of all putative pyramidal cells in either the LEFT or RIGHT running directions. The Posterior probability that a given ripple event represented either direction of run sequence was defined by:

$$Pr(dir \mid spikes) = \left(\prod_{i=1}^{n} f_i(dir)^{sp_i}\right) e^{-\tau\sum_{i=1}^{n} f_i(dir)} \quad (6)$$

Where $f_i(pos)$ is the value of the firing rate-by-direction vector of the i^{th} pyramidal cell for direction *dir*, sp^i is the number of spikes fired by the i^{th} pyramidal cell in the ripple event being decoded, τ is the duration of the event in seconds and *n* is the total number of pyramidal cells. Each linear-maze session event was first classified as either a 'LEFT' or 'RIGHT' event based on the maxima of *Pr(dir | spikes).* Events (from all sessions/mazes) with positive weighted correlations (that is, a positive correlation between decoded position and decoding bin time) were considered forward sequence events, while those with negative weighted correlations were considered reverse sequence events.

Separately, 1,000 *null* (shuffled) firing rate-by-position templates were constructed by circularly translating the un-smoothed firing rate by position vector by a random number of bins independently for each place cell, and re-smoothing ('*circular*

place-field shuffle'). This method was chosen as the primary shuffling approach because 1) it is only applied to the spatial templates (and not to any of the individual events), thereby not assuming the independence of firing structure between events, 2) it specifically degrades spatial coding without affecting many other of the cells' properties such as firing rate and firing rate variance. The full replay analysis (above) was performed using these 1,000 null templates leading to 1,000 *r(null)* values for each ripple event. For each event a *sequence score (rZ)* was defined as the absolute value of its weighted-correlation as a z-score relative to its expected absolute *null* weighted correlation distribution:

$$rZ = \frac{|r(observed)| - |\overline{r(null)}|}{\mathrm{S.D}(|r(null)|)} \quad (7)$$

Where S.D. is the standard deviation function. Note that this value does not distinguish between forward and backward replay events and is positive in cases where the observed $|r|$ value is greater than its expected (mean) absolute *null* value and negative otherwise.

A secondary 'time-bin-shuffle' (figs. S8, S22) was performed by permuting the order of the 20 ms time-bins within each event. One-thousand time bin shuffles (associated with 1,000 $r(null_{time\text{-}bin\text{-}shuffle})$ values) were created for each event. Note that while also preserving many of the observed spiking properties, such as per event firing rate and firing rate variance, this alternative *time-bin-shuffle* is distinct and complementary to our primary *circular place-field shuffle* in that it specifically degrades within-event temporal structure while preserving the observed place field templates.

Surrogate Data Sets

Two distinct classes of surrogate events were created: 1) Poisson surrogate data sets: each cell's within-ripple firing rate were modelled as Poisson spike trains with means equal to each cell's within-ripple event firing rate. Poisson means were estimated separately for each behavioral epoch, and running direction. 2) Time-bin-shuffle surrogate data sets: the order of the 20 ms time-bins within each event was randomly permuted within that event. One-hundred surrogate data sets of each these two classes were constructed – 200 shuffled controls were made for each these surrogate data sets.

Per Cell Contribution (PCC) Analysis

For each cell 1,000 partially shuffled place representation matrices were made in which only that cell's place representation was randomly shuffled (circularly translated as

described above). For each event that that cell participated (fired at least one spike) in, sequence scores (*rZ*) were assessed using these 1,000 cell-specific shuffled place representation matrices. For a given event '*e'* a given cell's ('*c')* contribution was estimated as the average putative 'degradation' of sequence content caused by the specific degradation (shuffling) of that cell's spatial coding, normalized by the number of participating cells in this event:

$$PCC_{e,c} = \left[(rZ_e(observed) - rZ_{e,c}(cell\ c\ shuffle) \right] \times \#Participants_e \quad (8)$$

Where *'#Participants$_e$'* indicates the number of place cells that fired at least one spike in event *e*. The multiplication by the number of participants corrects for the proportionally larger influence each cell may have on sequence content in events with few participating cells (fig. S10). Each cell's PRE PCC score was assessed as its mean contribution across all PRE ripple events it participated in, while it's POST PCC score was assessed as its mean contribution across all POST events.

To confirm our main PCC results obtained by circular-place field rotations an alternative PCC analysis (PCC_{TBS}; fig. S22) was performed by randomly permuting the firing-rate by time-bin vectors within each ripple-event independently for each place cell. This cell-specific time-bin-shuffle (TBS) was performed 1,000 times for each cell and event, and cell-specific *r(cell shuffle)* values were computed for each. The rest of the PCC_{TBS} analysis was performed as above with the exception that the (none-cell-specific) time-bin-shuffle - rather than the circular place field shuffle - was used to generate values of *r(null).*

To assess the contribution of place cells with different degrees of PRE to POST change in PCC to the observed overall changes in sequence content from the PRE to POST, two separate analysis were carried out. In the first (Fig. 2C) the full Bayesian replay analysis was performed with place field templates (n = 1,000 each) in which an increasing number place cells' place fields were shuffled, starting either with cells with low or high ΔPCC values. In the second analysis (fig. S8), the replay analysis was repeated after excluding from analysis either cells with increasing or decreasing ΔPCC values. Importantly, since in different sessions differing numbers of place cells were recorded, in these analyses (as well as in all other analyses in which cells were excluded) the selection of cells to be excluded or shuffled (respectively) was performed *within each session* and the results were then pooled across sessions. Note that the cell exclusion analysis was only carried out to 75% of cells because after this point not all sessions met the criteria for contributing to the analysis (at least 5 place cells active/event).

Synthetic Sequence Model

The PCC method was tested on a deterministic synthetic model approximating 'perfect' sequence content. This pared-down model was designed to test the assumptions of the PCC method explicitly on a 'ground truth' synthetic data set in which sequence content could be deterministically set, rather than as a model of physiological virtual sequence content. In this model, synthetic firing-rate-by-position templates were constructed such that each of *n* participating place cells had one place field, and place fields peaks linearly spanned the 2-meter (100 bin) 'virtual maze' (i.e., for each bin there was a place cell with a place field). All place fields had equal place field peak firing rates and widths empirically matched to the medians of the recorded data (place field peak: 5.01Hz, place field width: 24 cm). Likewise, corresponding 'synthetic ripple events' of length *d* (where *d* was as a multiple of the 20 ms bins size) were constructed such that each of *n* participating place cells each fired 1 spike linearly spanning the event (from time 0 to time *d*) and corresponding to the order of their place field peaks in the synthetic place field template. The free parameters *n* participating cells and *d* event duration were densely sampled to match the recorded data. Bayesian decoding, weighted correlation and PCC analysis were performed as described above.

Rigid and Plastic Cell Classification

For each cell and behavioral epoch the hypothesis that 'the shuffling of that place cell's place field decreased the amount of observed sequence content in those ripples within which it fired' was tested by performing a one-tailed Wilcoxin Rank-Sum test over that place cell's per-event PCC scores. Those cells showing significant PCC values ($p < 0.05$) in either PRE or POST epochs were considered to be *strongly contributing* to sequence content. For each session and running direction the strongly contributing cells equal to or below the 50th percentile of that session's ΔPCC were considered *rigid cells* (n = 105 cells, blue x's), while the strongly contributing cells above the 50th percentile of that session's ΔPCC distribution were considered *plastic cells* (n = 105 cells; for sessions with an odd number of strongly contributing cells the cell with the median ΔPCC value was excluded). This selection method was chosen as a conservative approach which ensures that a) plastic cells were the subset of cells that showed the greatest increase in their POST compared to PRE contribution, b) all rigid or plastic cells contributed strongly to at least one of the phenomena of interest (i.e. PRE and/or POST sequence content), c) each session contributed an identical number of rigid and plastic cells. However, while this binary classification was made in order to facilitate a conservative description of the phenomenon, we emphasize that the distribution of PCC or ΔPCC

values, though skewed, was not bi-modal. Furthermore, we do not exclude the possibility that in certain experimental conditions or individual sessions, a greater or smaller proportion of cells may show 'rigid' or 'plastic' characteristics – which would not be captured by the '50-50' split employed here. Therefore, we emphasize that our approach should be understood as a conservative method for investigating two ends of continuous distribution. In future works, less conservative and perhaps more sensitive classification methods can be used for addressing the role and significance of this continuous distribution.

Pair-Wise Temporal Interaction Analysis

Cross-corellograms (CCG's) with a half-width of 150 ms were constructed for all pairs of place cells during 'off-line' states during the PRE or POST epochs, or during active running (>5 cm/s) epochs during novel maze running. For each pair of cells a 'CCG bias' was defined as the sum of all the co-incident spikes in which the reference cell fired after the comparison cell minus the sum of all the co-incident spikes in which the reference cell fired before the comparison cell, divided by the total number of co-incident spikes (*34*). Cell pairs recorded on the same shank, or which fired fewer than 40 coincident spikes in either of the conditions being tested were excluded from the analysis. The Pearson correlation coefficient was taken as the similarity between the temporal bias patterns between epochs. Since for each pair the identity of the 'comparison' and 'reference' cells, and hence the sign of each pair's temporal bias, could be arbitrarily assigned by the experimenter, the signs (but not the magnitudes) of each pair's temporal bias was randomized independently across pairs but consistently across epochs. The correlation measures were performed independently on each of these thousand randomly referenced data sets. The reported correlation values were defined as the median correlation coefficient (and associated p-value) across all 1,000 permuted data sets.

Pair-Wise Co-Activity Analysis

For each place cell firing rate vectors were constructed using 100-ms non-overlapping bins during 'off-line' states (quite immobility and NREM) independently in the PRE and POST epochs, as well as during active Maze running (>5cm/s). Pair-wise co-activation values were taken as the Pearson's correlation coefficients between the firing rate vectors of all pairs of place cells for the PRE and POST epochs. Pairs of place cells recorded on the same shank were excluded from the analysis.

Paired-Latency Analysis

To test our findings independently with a template-based method which did not rely on Bayesian decoding, a 'Paired-Latency' measure was derived. This measure is similar to the 'Rank ordered correlation method' (*3, 4, 18*) but, amongst other advantages, has the feature of being able to exclude the effect of pairs recorded on the same silicon probe shank.

For the paired-latency analysis only ripple events with durations of at least 100 ms and in which at least 10% or 5 (whichever was greater) of place cells fired were included. For a given event with n active and inactive cells, a paired latency vector PL of length $(n)(n-1)/2$ corresponding to the number of unique non-self pairs was constructed. For each cell active in each event a 'within-event spike timing' value was assessed as the center of mass of all the spikes that that cell discharged within that event, relative to the center of mass of all the spikes fired by pyramidal cells within that event. For each comparison, one cell was chosen as the reference and the other as the comparison – the choice of which cell of the pair is the reference and which the comparison is arbitrary but must be applied consistently across all events and conditions. Any given element (corresponding to a given non-self cell pair) of the paired latency vector PL was assigned one of three possible values:

1 If the comparison cell's within-event center of mass of spiking (c.o.m.) occurred after the reference cell's within-event c.o.m.

-1 If the comparison cell's within-event c.o.m. occurred before the reference cell's within-event c.o.m.

0 If the two members of the pair had the same within-event c.o.m., if either member of the pair did not fire in the event, or if both members of the pair were recorded on the same shank

Paired distance, PD, vectors were similarly constructed from the relationship between linearized place field peaks (only the location the highest place field peak was used for this analysis) such that each element of the PD vector had one of three possible values:

1 If the comparison cell's place field was to the right of the reference cell's place field

-1 If the comparison cell's place field was to the left of the reference cell's place field

0 if the place field peaks of both members of the pair occurred on the same bin, if either member of the pair was not a place cell or if both members of the pair were recorded on the same shank

For linear maze sessions separate PD vectors were constructed for left and right directions of movement. Note that starting from these vectors it is possible to fully reconstruct rank-ordered sequence content. The null distribution was estimated using 1,000 PD vectors constructed by shuffling (resampling without replacement) of place cell ID's.

For a given event *e* the similarity of within-event sequence to the order of place fields on the maze was calculated as the dot product of PD and PL_e divided by the dot product of the absolute values of PD and PL_e:

$$Seq_{PL} = \frac{PL_e \cdot PD}{|PL_e| \cdot |PD|} \qquad (10)$$

In other words, the sum of all the non-zero elements which had the same non-zero value in both PL and PD minus the sum of all elements that had different non-zero values normalized by the sum of the elements that were non-zero in both PL and PD. This value is a measure of order similarity and is bounded between -1 (when one sequence is the reverse of the other) to 1 (when the two sequences being compared are the same).

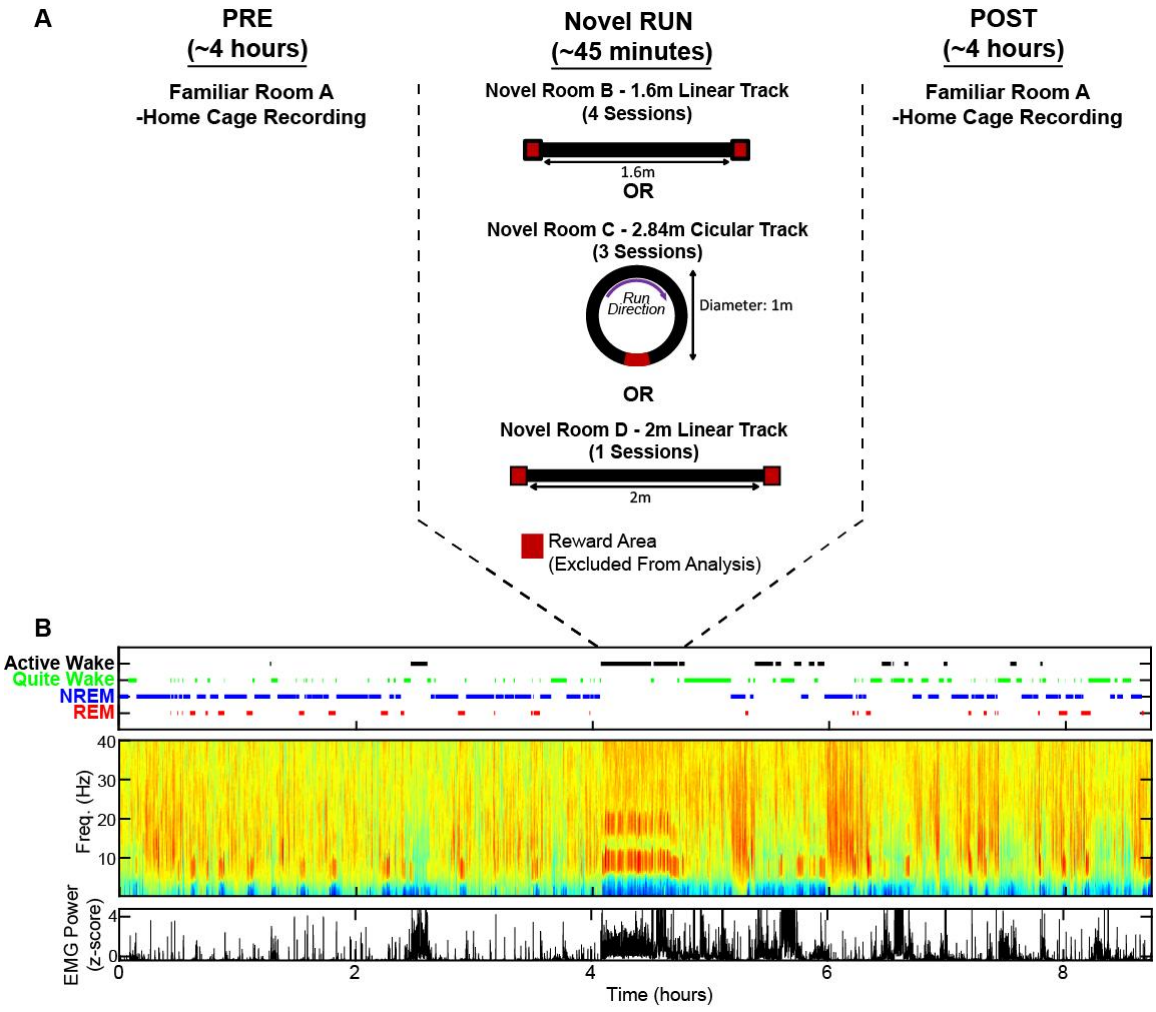

Fig S1: Behavioral and recording paradigm. (**A**) Each recording session consisted of three phases: 1) a long (~4 hour) PRE epoch in which the animal was allowed to rest or sleep in its homecage in familiar room A, 2) the animal was subsequently transferred to one of three rooms it had never previously been exposed to, and rewarded for running on a novel maze (MAZE), 3) the animal was returned to its homecage in room A for another long (~4 hour) POST sleep/rest recording. Note that the reward areas (red) of each maze were excluded from the analyses (the dimensions shown for each maze reflect the linearized lengths after the exclusion of the reward areas). **(B)** PRE, MAZE and POST epoch sequence content was only assessed during ripple events occurring during quiet immobile waking (green) or NREM sleep epochs (blue) as determined by hippocampal CA1 pyramidal LFP spectrograms and simultaneous electromyographic (EMG) recordings.

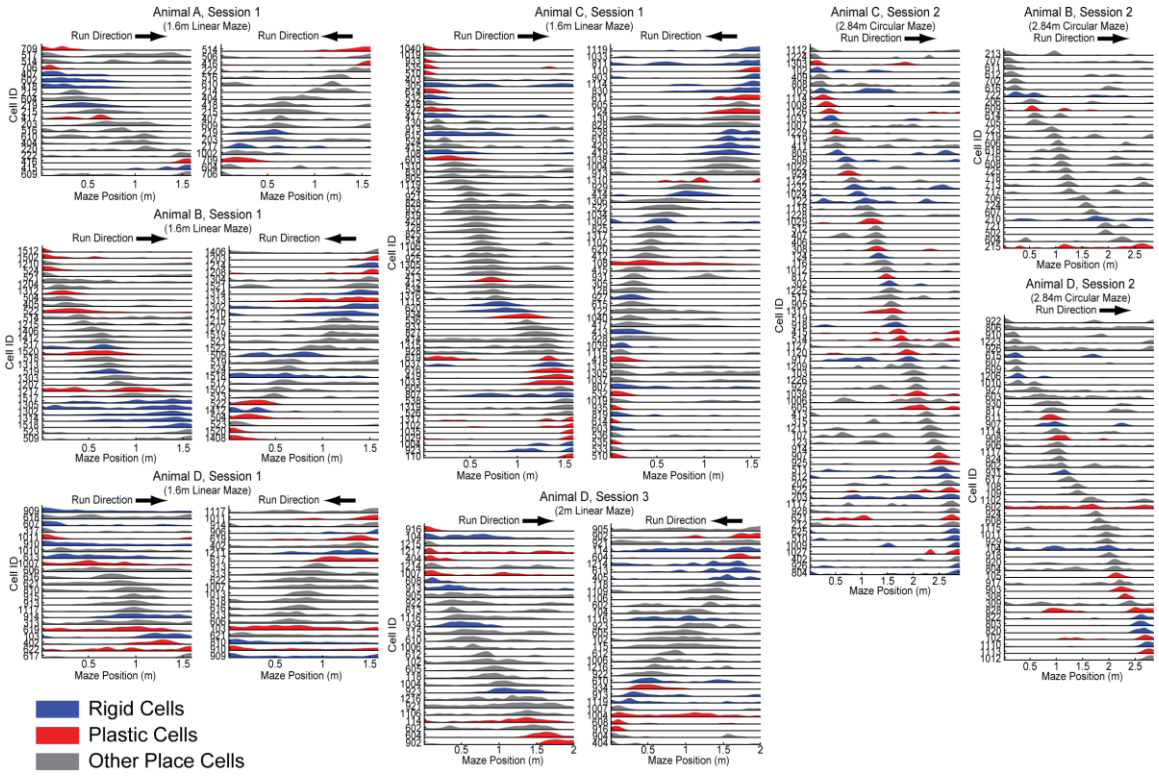

Fig. S2: Place fields on novel mazes. The spatial receptive fields (place fields, n = 491) of all recorded place cells are shown. Consistent with the analysis, cells which had place fields (see Methods) on both directions of the linear maze are plotted independently in each of these directions. Circular maze sessions (right 2 columns) were linearized with the origin corresponding to the leading edge of the reward area. Note that the place fields of rigid (blue) and plastic cells (red) are similarly enriched near the start and goal ends of the track.

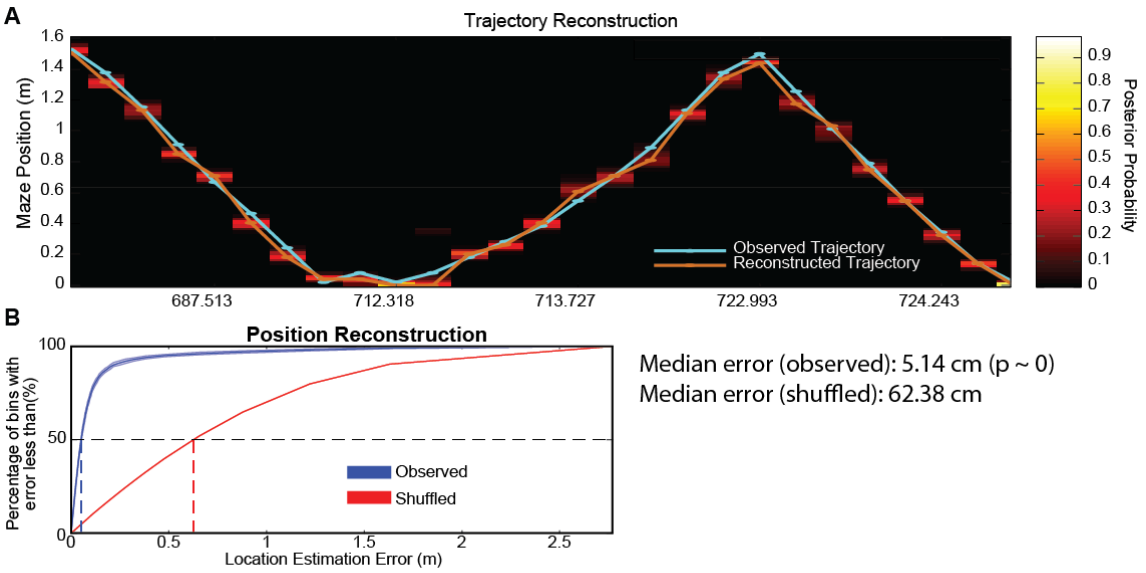

Fig. S3: Bayesian firing sequence reconstruction. For each running direction, the firing rate by position vectors across all place cells was used to build a Bayesian decoder of location by place cell firing rate. For validation of the decoder, place field spiking was binned in non-overlapping 500ms bins during active maze running (speed 5 > cm/s), and used to decode the animal's position. The top panel shows the decoding of 3 laps (two incoming and one outgoing) of linear maze running. Each row corresponds to one 500 ms bin, the background (heat-map) colors show the decoded posterior probability that the spiking data represented a given location (y-axis) at a given 500ms bin (x-axis). The copper line shows the path along the maximum posterior probability (predicted position) at each bin, while the cyan line shows the observed trajectory of the animal as determined by LED tracking. The bottom panel shows the cumulative distribution curve for the position estimation errors across all 500 ms bins in all sessions, while the red shows the equivalent curve derived from 1,000 shuffled place field vectors. The shuffling here, as in the rest of the work, was performed by circularly translating the un-smoothed firing rate by position vector by a random number of bins independently for each place cell, and re-smoothing.

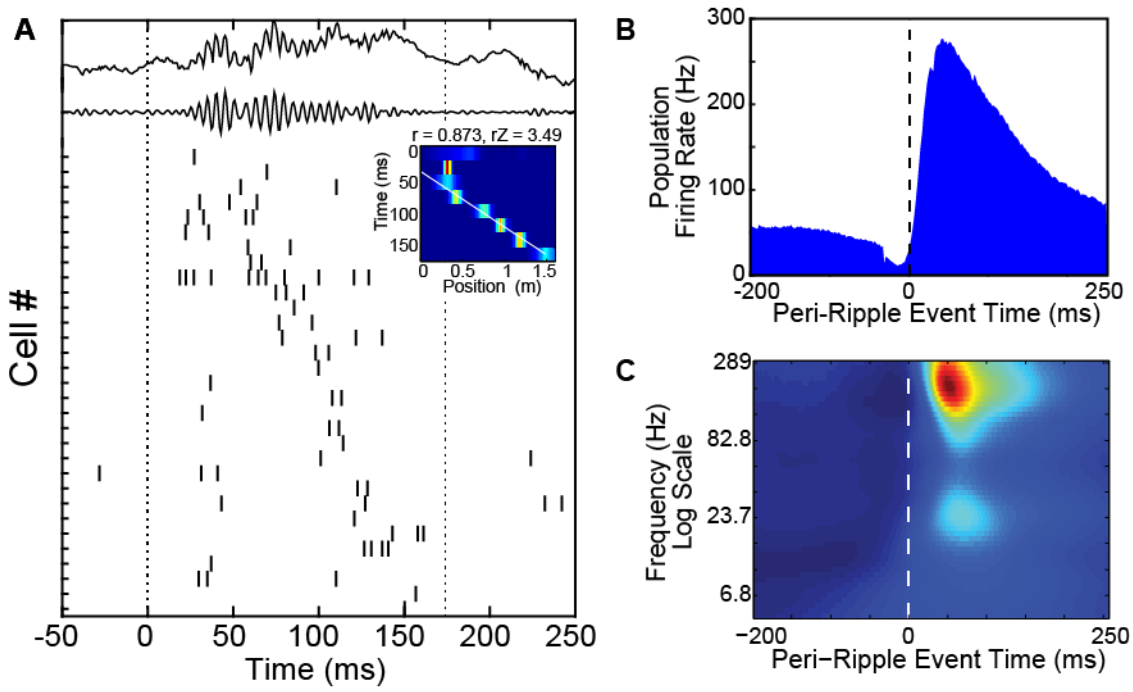

Fig. S4: Ripple events were detected as the coincidence of the synchronous firing of the pyramidal cell population and LFP-detected sharp-wave-ripples. (**A**) A sample POST epoch replay event, showing the wide-band CA1 pyramidal layer LFP (top), the ripple-frequency (150-250Hz) filtered LFP, and the spiking activity rasters of the 32 place cells active in the event. The vertical dashed lines show the beginning and end time points of the ripple event. The inset shows the Bayesian 'virtual travel' decoded from this event. Ripple event triggered pyramidal cell population firing rate (**B**), and spectral decomposition of the CA1 pyramidal layer LFP (**C**).

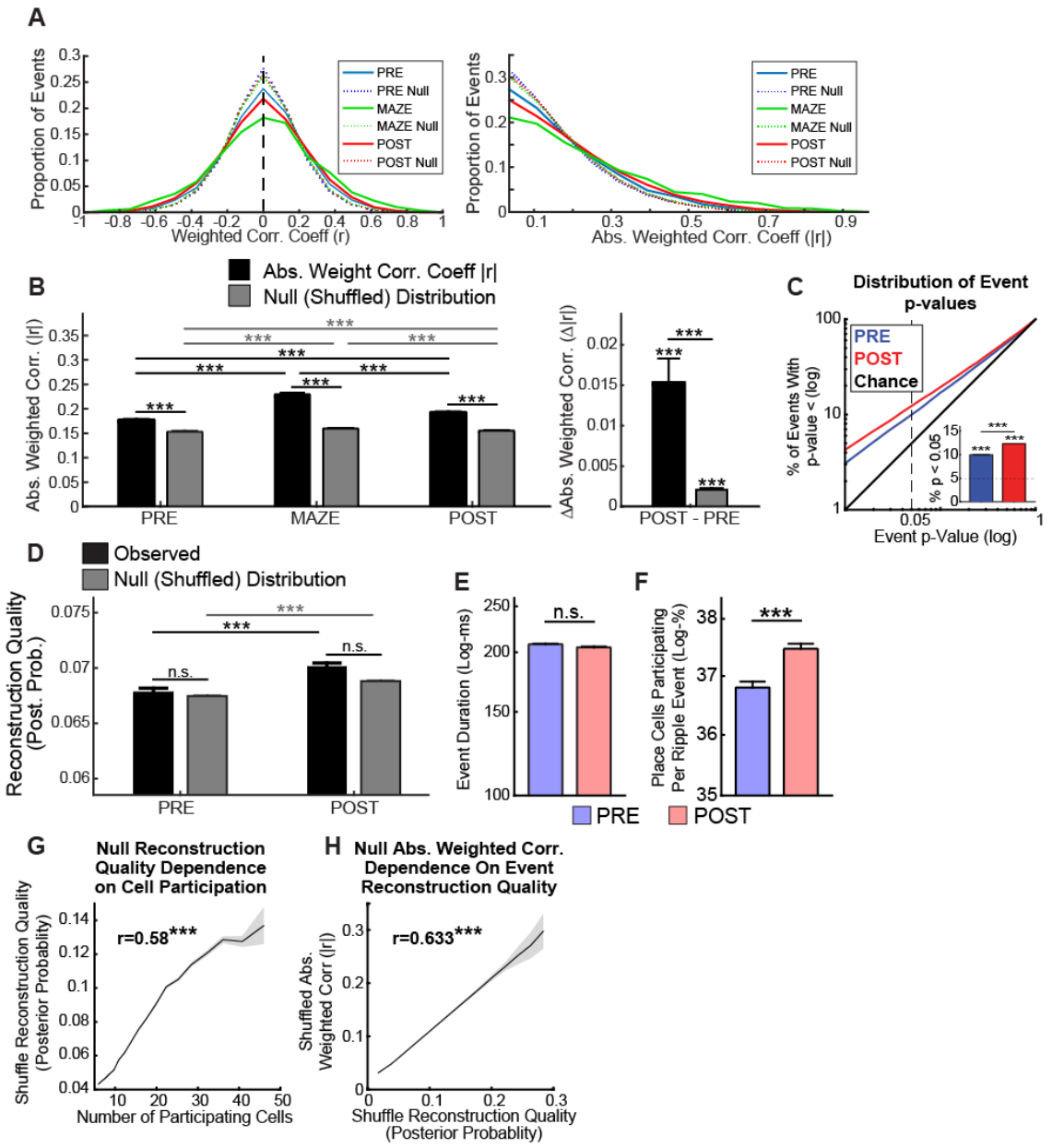

Fig. S5: Sequence content increases from PRE to POST. (A) Distribution of weighted correlation coefficients (none-normalized sequence content, left panel) and absolute weighted correlation coefficients (right panel). Note the higher tail values of experiments compared to the shuffled null distributions (see *Methods*). **(B)** Observed absolute weighted correlation coefficients against the values expected from shuffled place field vectors (see *Methods*, within condition between epoch significance testing: Kruskal-Wallis, followed by post-hoc Tukey-Kramer tests; between condition within epoch testing: Rank-Sum tests). **(B)**, right panel, POST – PRE change of absolute weighted correlation coefficients (graphs show the POST – PRE means ±SE, significance tested via boot-strap test). Note that in all three epochs, a greater degree of sequence content is observed than expected by chance. Note also that the absolute value of the null (shuffled) distribution increases significantly from the PRE to the POST epochs (and also varies

between events) – necessitating a normalization by the varying null statistics which was accomplished by computing the normalized rZ scores (see *Methods*). **(C)** cumulative distribution of p-values (relative to each event's null distribution drawn from 1,000 shuffled place templates) for events in the PRE (blue) or POST (red) epochs. Inset, percentage of events in either PRE or POST epochs with p-values less than 0.05 (statistical testing: chi-square test of proportions). The 'observed' and circularly-shuffled templates did not significantly differ in many of their properties, including each cell's estimated spatial information per spike (data not shown, see *Methods*). For each observed and shuffled event, the reconstruction quality of the Bayesian decoder was measured as the median across time bins of the maximum Bayesian posterior probability value in each time bin. **(D)** Note that reconstruction qualities are not significantly different between observed and shuffled events in either the PRE or POST. This is important as the expected null absolute weighted correlation coefficient is strongly dependent on the reconstruction quality (approaching zero as the posterior probability distribution becomes flat). **(E)** While ripple-event duration did not differ between the PRE and POST epochs (PRE median duration 183ms, POST median duration 186ms, $p < 0.07$, Rank-Sum test), **(F)** a significantly greater percentage of place cells participated (fired at least one spike in) POST epoch events. Note that the changing participation statistics may account for the observed change in the PRE to POST null (shuffled) absolute weighted correlation (B, grey bars). (**G)** For each event (here pooled across PRE, MAZE and POST epochs), the number of participating cells was plotted against the mean of its shuffled reconstruction quality values (plot shows mean ±SE, r-value from Pearson's correlation). **(H)** In turn, increases in reconstruction quality typically (though not necessarily, see figure S7) associated with a greater number of participating cells result in increases in absolute weighted correlation coefficients independently of temporal structure.

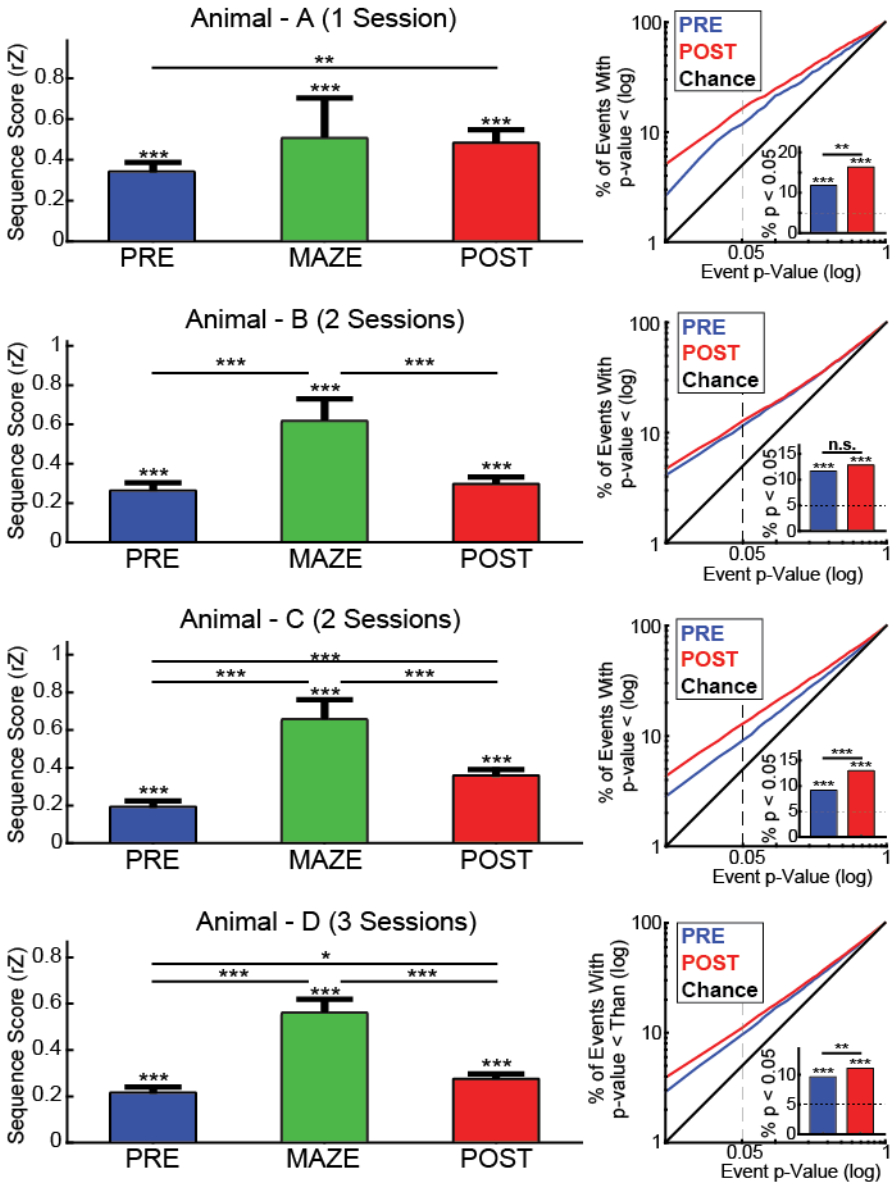

Fig. S6: Sequence scores and Associated p-values computed in each animal separately. Sequence scores summarized as in Figure 1C inset, p-value graphs as in fig. S5, C.

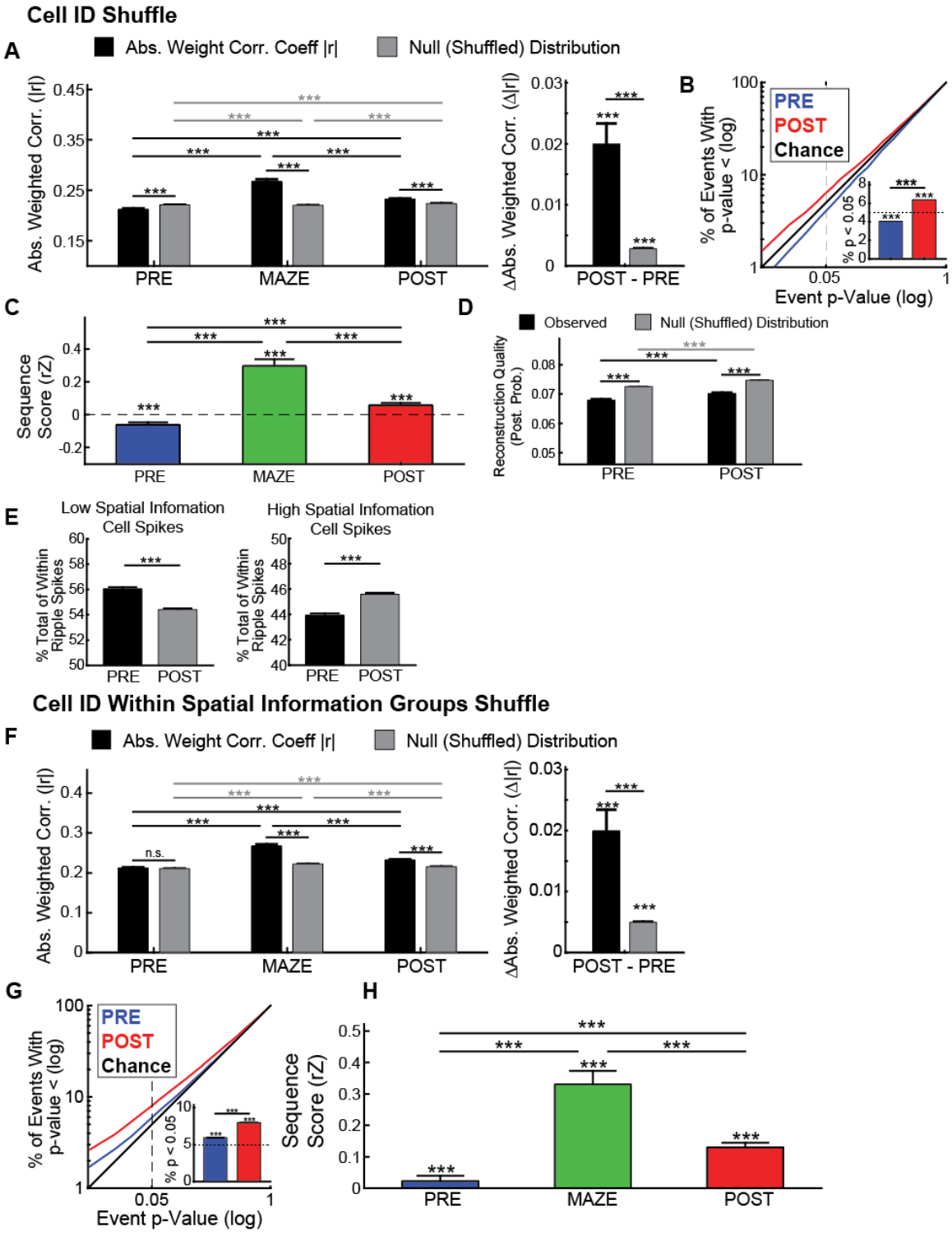

Fig. S7: Estimation of sequence content is sensitive to the choice of null distribution for Bayesian analysis. (**A-C**) As an alternative to our standard shuffling approach (circular translation of place fields), we recomputed a separate null distribution in which each place cell's ID was randomly shuffled (1,000 shuffled templates constructed by resampling without replacement). Under this shuffling approach POST and MAZE

trajectory content (as well as the POST – PRE change) were found to be significantly different than their null values (left and middle panels). POST was also found to have significantly more $p < 0.05$ events than expected under null assumptions (**B**, red column in inset, right panel). However, PRE sequence content was found to be significantly smaller than the PRE-null distribution (**A**, left column-pair, Rank-Sum test, $p \sim 0$). Consistent with this finding, we observed that PRE displayed significantly fewer $p < 0.05$ events than expected by chance (**B**, inset, blue bars, Chi-Square test). (**C**) The rZ scores associated with PRE were also found to be significantly negative (**C**, blue column). In other words, under each of these tests the PRE was found to have 'negative preplay' (*18*, *19*), that is, less sequence content than would be expected by chance under the assumptions of the cell ID shuffle. We hypothesized that this was the result of the fact that the distributions of cell activity change from the PRE to the POST epochs. In particular, it was hypothesized that the cell-ID shuffle over-estimated the relative contribution of sparsely firing high-spatial information content cells (that is that high-spatial information, 'peaky' , spatial templates were used to decode, on average, more spikes and hence led to 'peakier' Bayesian reconstructions in the cell-ID shuffles than in the experimental data). (**D**) Consistent with this hypothesis the cell-ID shuffled data displayed markedly higher Bayesian reconstruction quality (a measure of the 'peakiness' of the Bayesian posteriors). Note that the 'peakiness' of Bayesian reconstructions are strongly correlated with higher expected abs. weighted correlation values even in the absence of sequence structure (see fig. S5, panel H). In order to examine this hypothesis cells were split (along the median value, within each session and running direction) into two equal groups of 'Low Spatial Information' and 'High Spatial Information' neurons. Spatial information is relevant in the current context because the reconstruction quality ('peakiness') of the posterior probability estimates derived from the commonly used Bayesian decoder employed in the current study tends to be more influenced by the activity of high than low spatial information cells (this property, in fact is one of the reasons it is particularly well-suited for position decoding). (**E**) Consistent with our hypothesis, low spatial information content cells were found to account for a higher percentage of all within-ripple spiking in the PRE compared to POST epochs, while the inverse was true of the high spatial information cells (graphs show mean ±SE across all PRE or POST epoch events, Rank-Sum test). (**F-H**) In order to test whether this relationship could account for the 'negative preplay' anomaly, cell ID's where shuffled within the low or high spatial information cell groups (but not between them). Importantly, while also accomplished by shuffling the Cell ID's, the 'spatial information controlled-shuffle' may be regarded as more conservative, since this shuffling procedure has many fewer degrees of freedom and, thus, the resulting shuffled templates will tend, on average, to be more similar to the original template. While the comparison of the entire observed PRE to PRE-null distributions did not show a significant difference (**F**, left column-pair, Rank-Sum test) - a significant number of PRE events were found to have p-values < 0.05 (**G**). Furthermore, the computed PRE-rZ values (**H**) were also found to be significant (Sign-Rank test). Importantly, the commonality between the p-value and rZ test methods is that in both of these events' observed trajectory content is compared to its particular null distribution. Consequently, we conclude that in this, highly conservatively shuffled, case the lack of significance observed when employing the entire PRE to null distributions may be attributable to the fact that some events have wider null

distributions than others and these events ‘populate’ the null with higher values, potentially leading to a false failure to reject the null - this is analogous to the increased statistical power derived from using paired versus unpaired tests of significance. In summary, differing null assumptions can lead to strikingly different statistical results. Therefore, it is important to emphasize that shuffling procedures which assume the interchangeability of cells, and consequently do not replicate the variance in coding and excitability properties observed across cells, may lead to potentially invalid or paradoxical conclusions.

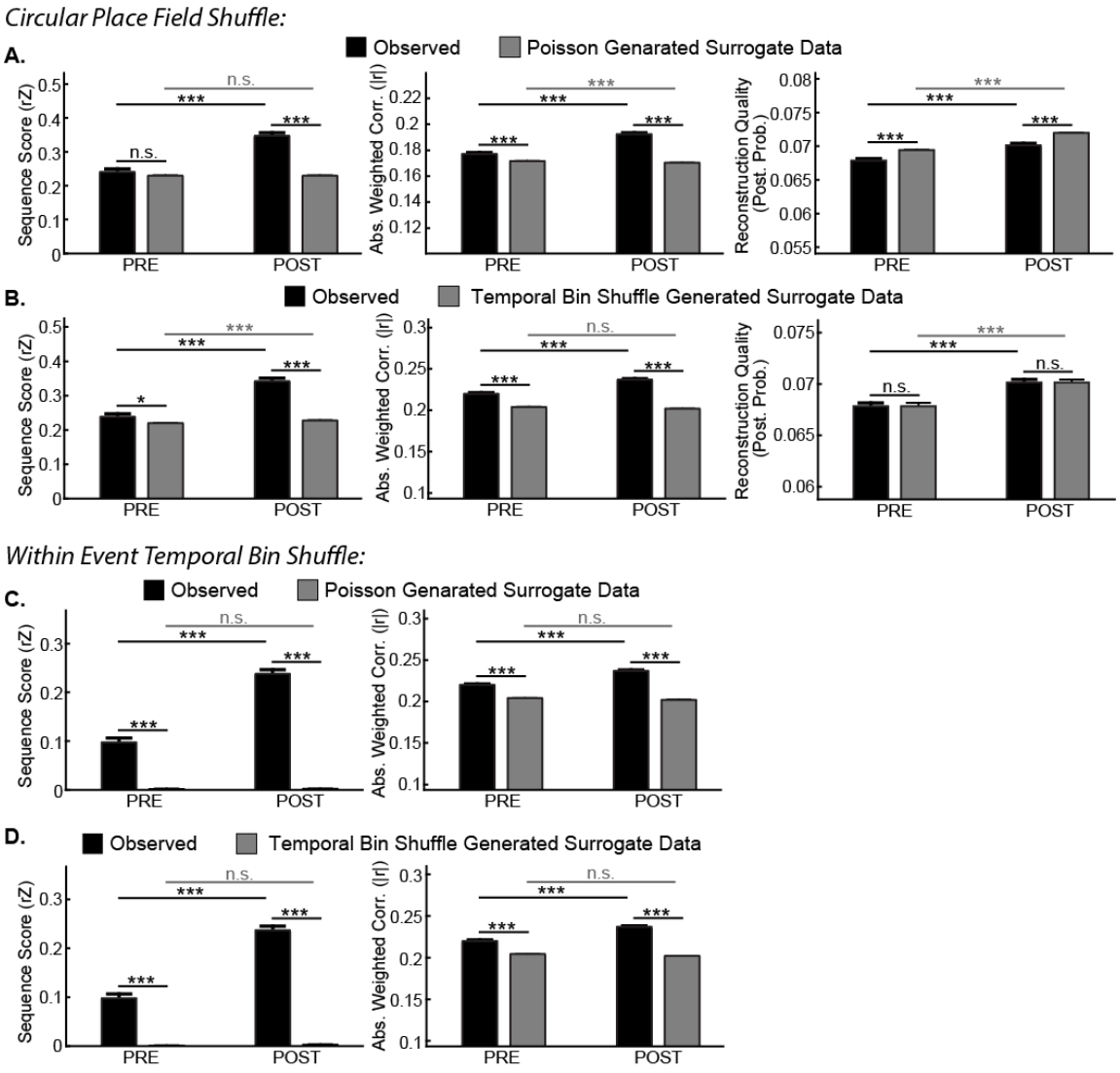

Fig. S8. Comparison of observed and surrogate data. In order to further test putative sources of structure in the data, Bayesian analysis was compared between observed and Poisson-generated surrogate data (100 surrogate data sets per condition). For the observed and each of the surrogate data sets, null (shuffled) data sets were constructed using the 'circular place-field shuffle' (n = 200 shuffles per data set). (**A**, left-panel) Consistent with a previous report (*14*) we found that the normalized sequence score (rZ) was significantly different between observed and Poisson-surrogate data during the POST but not the PRE epoch. This result implies that that PRE-observed and PRE-Poisson were not distinguishable in terms of their sequence structure. (**A,** middle-panel) However, when the absolute weighted correlation values were compared between the observed and Poisson-surrogate data, both their PRE and POST epochs were found to have a higher degree of structure than their Poisson-surrogates. (**A,** right-panel) Note that this was the case despite the fact that the surrogate data set showed significantly higher Reconstruction Quality (a measure of the 'peakiness' of the Bayesian Posterior Probability distribution) in both the PRE and POST epochs – which would be expected, in the absence of further structure, to lead to higher absolute weighted correlation scores

(see figure S5H). The difference in sequence content and/or reconstruction quality between the observed and Poisson-surrogates is potentially due to the fact that within-ripple spiking is highly non-stationary both across bins and ripple-events and hence none-Poisson (observed PRE-epoch within-ripple inter-spike-interval (ISI) Coefficient of Variation (CV): 1.39, $p < 0$, Signed-Rank test across place cells against a null value of 1 as would be expected by a Poisson distribution, POST ISI CV: 1.37, $p < 0$). **(B)** In order to more closely approximate the observed firing statistics, separate surrogate data sets were constructed by randomly permuting the 20-ms time-bins within each event (100 time-bin-shuffle surrogates). Using this more conservative surrogate procedure revealed significant differences in sequence scores (left-panel), and absolute weighted correlation coefficients (middle-panel) between the observed and TBS-surrogate data in both PRE and POST. Note that this surrogate method more closely approximates the observed firing statistics, preserving, for instance, the observed Reconstruction Quality (right-panel). As an alternative to the 'circular place-field shuffle' used in **A** and **B**, the observed as well as Poisson and time-bin-shuffle surrogate data sets were compared against time-bin-shuffle null-distributions (see *Methods*). Using this shuffling technique, sequence scores and absolute weighted correlation coefficients were found to be greater in the observed PRE and POST than in both the Poisson (**C**) and time-bin-shuffle (**D**) generated surrogates. Together, these results suggest that some, though not all, of the putative PRE structure may be explained through first-order relationships between cell's firing rates in PRE epoch events and the structure of place fields on the novel maze. This issue needs further exploration in future research.

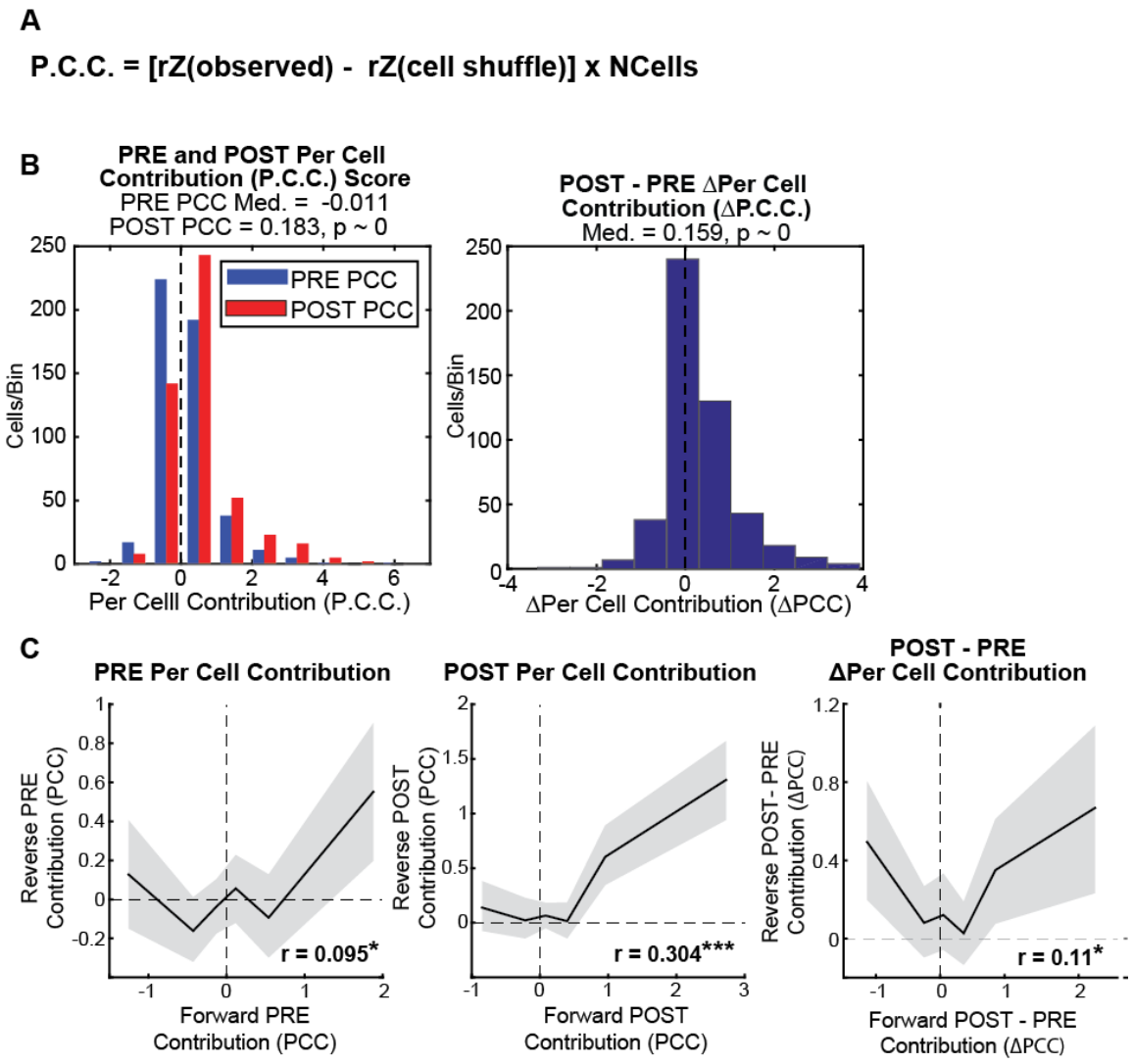

Fig. S9: Per Cell Contribution (PCC) to sequence content. (**A**) For each place cell, PCC was measured as the putative 'degradation' in the observed sequence score (*rZ(observed)*) resulting from the specific shuffling of that cell's spatial receptive field template (*rZ(cell shuffle)*). This quantity was multiplied by the total number of cells participating in each event to account for the fact that each cell's ability to degrade an event's virtual travel content is inversely proportional to the number of cells participating in that event (see fig. S10). (**B**) For each neuron, PRE and POST PCC scores were taken as the mean across all ripple events that that cell participated (fired at least one spike) in in each of these epochs. (**B**, left panel) PRE and POST PCC scores are shown for all place cells (n = 491). The panel title indicates the median for each of the two distributions (p-value from rank-sum test). (**B**, right panel) The distribution of ΔPCC (POST - PRE PCC) values is shown for all place cells, the panel title shows the median ΔPCC score (p-value from signed-rank test). Note that consistent with the main Δreplay effect (Fig. 1C, POST > PRE sequence scores (rZ)), cells show significantly higher POST, compared to PRE PCC scores. (**C**) Forward and reverse PCC scores were independently computed from ripple events with forward or reverse virtual travels. For linear mazes each ripple event was first assigned to a particular one of the two running directions by a Bayesian

decoder (see methods) ensuring that each ripple event was only considered once as either a reverse (weighted correlation < 0) or forward (weighted correlation > 0) event. The panels show the Spearman's correlation coefficients between forward and reverse PRE PCC, POST PCC, or POST - PRE ΔPCC respectively. For these graphs, cells were divided into 6 equal, non-overlapping, subgroups by the by the Forward PCC shown on the x-ordinate, lines show the mean ±SE of the Reverse PCC scores indicated on the y-ordinate.

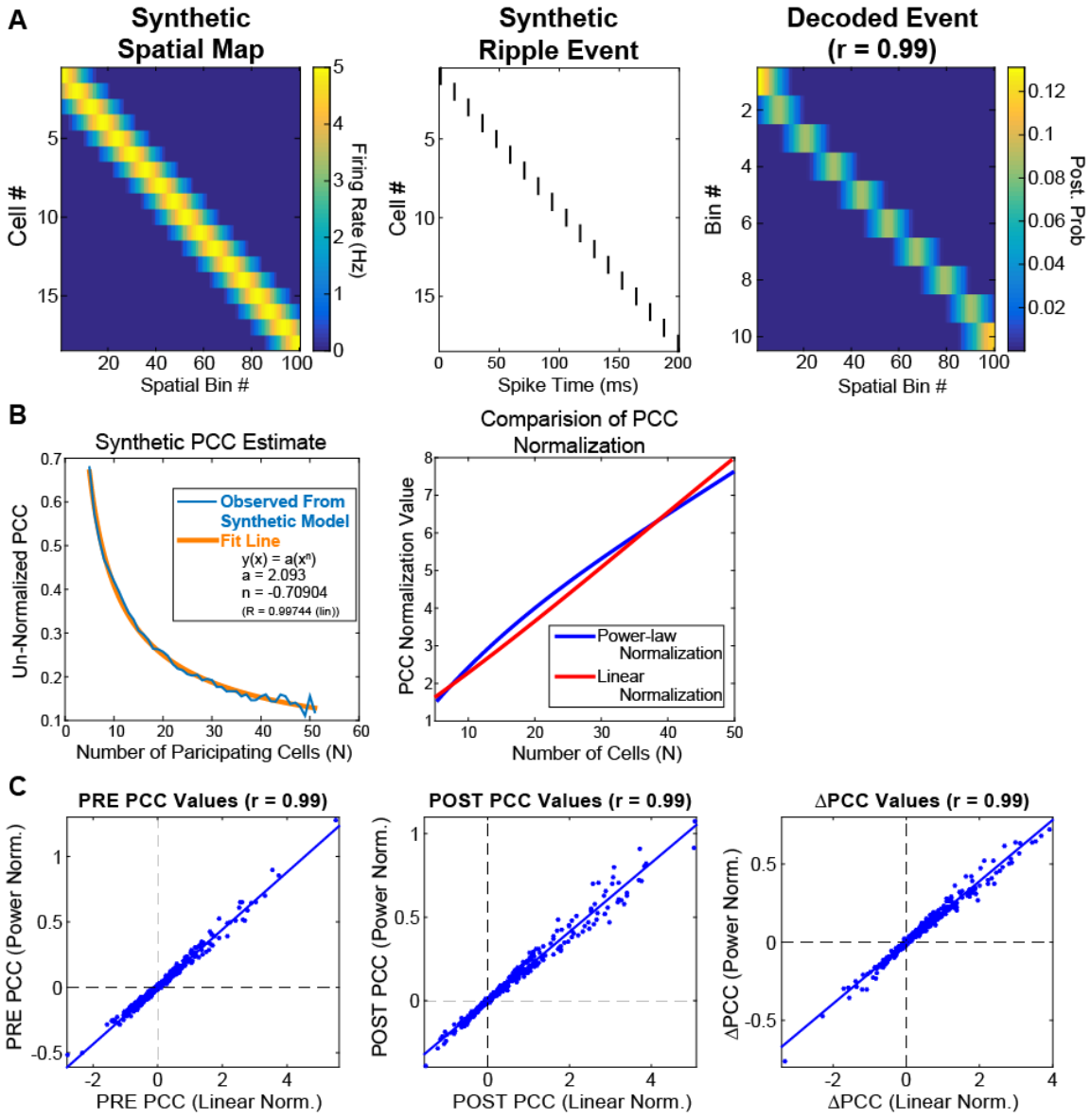

Fig. S10: Synthetic model of per cell participation. In order to test the assumptions made for deriving the PCC measure, a synthetic model of sequence content was developed. In this model, synthetic 'place cells' evenly spanned the maze (**A,** left panel) and fired one spike (**A**, middle panel) timed to correspond to the peak 'place field' firing rate. The synthetic ripple events were decoded with the synthetic place field maps resulting in 'perfect' sequence scores (that is, weighted correlation coefficients approaching 1, **A**, right panel). This model had two free parameters: the number of participating cells and the number of 20 ms bins making up the synthetic ripple events – panel **A** shows one example with 18 participating cells, and 10 temporal bins (corresponding to an event length of 200ms). Both the participant number and temporal bin number parameters were sampled densely to match the observed distributions (including all PRE, MAZE, and POST events). PCC analysis (see *Methods*) was carried out on these synthetic maps/events – note that since in this case all cells display 'perfect' sequence content, the estimated PCC for each one should be equal, regardless of the total

number of participating cells. **B.** When the PCC analysis was carried out (in this case without normalizing by the number of participating cells), a clear negative relationship was observed between number of participants and the estimated un-normalized PCC content, as expected. This relationship was well fit by a line following a power-law as a function of number of participants. Note that the resulting normalization function (i.e. the inverse of this power-law relationship) is well approximated by a linear relationship (**B,** right panel). In panel **C**, the results were compared between the application of either the power-law normalization (derived from our synthetic model) or the linear normalization used in the rest of the text**.** The r-values in the panel titles display the Pearson's correlation coefficients of the PCC values resulting from the two normalizations. Note that the PCC estimates are largely invariant with respect to choice of normalization – and this choice does not affect our findings (data not shown). Consequently, the simpler, linear normalization was adopted.

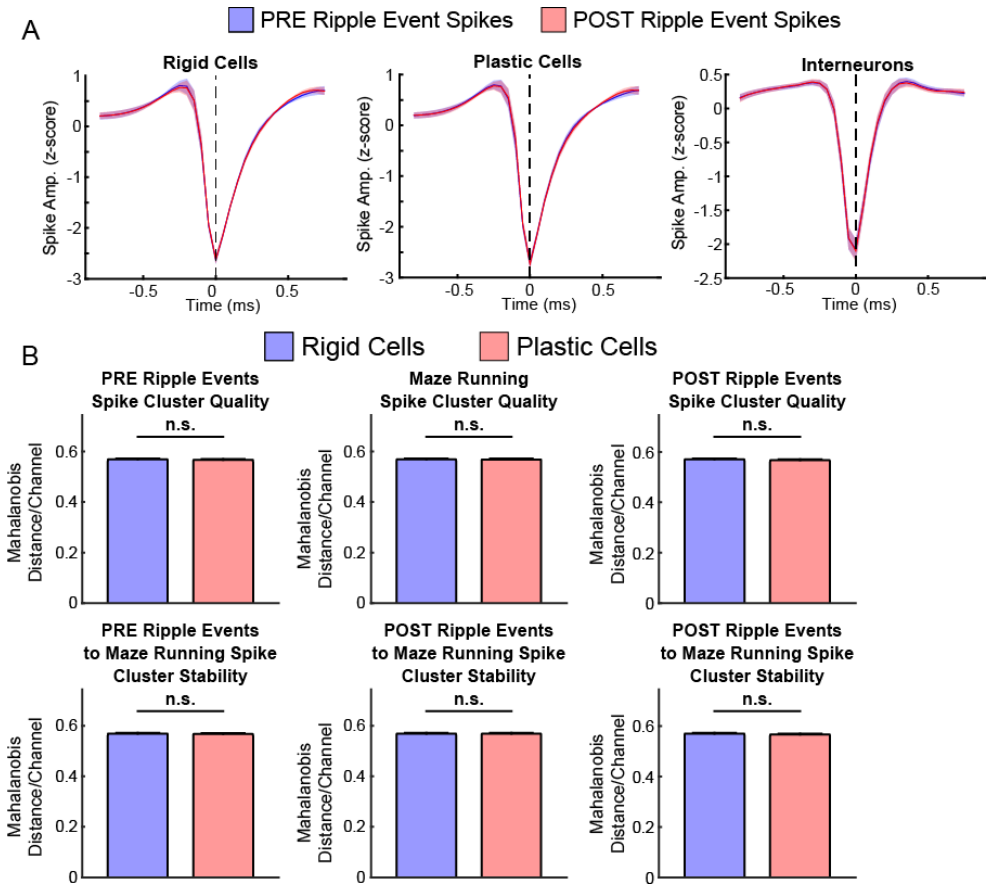

Fig. S11: Rigid and plastic cell cluster quality and stability. (**A**) The PRE and POST epoch within-ripple event waveforms are shown for rigid (left, n = 105) and plastic (middle, n = 105) cells. For comparison the waveforms of the interneurons recorded in our data set is also shown (right, n = 128 cells). Note that while rigid and plastic cell waveforms were similar, interneurons were contrasted by (amongst other features) narrower spikes and a more pronounced AHP's. For each cell the site displaying the maximal peak to trough range was normalized as the z-score relative to all unit and multi-unit activity at that site. The mean ± SE is shown for each cell class and condition. Note that rigid and plastic cell waveforms are similar to each other and stable from the PRE to the POST epochs. Cell cluster quality was taken for spikes occurring either during PRE ripple events (**B**, top left), MAZE active running (**B**, top middle) or during POST ripple events as the median Mahalanobis distance between the PCA features (used in clustering) associated with each spike and the center of the cluster (the mean across all spikes; (*29*)). For two conditions spike stability was measured as the symmetrical Mahalanobis distance between the feature cluster in one condition and the center of the cluster in the second condition. Since bursting is known to affect spike-shape properties (35), only the first spike of bursts (sequences of spikes occurring within < 6 ms of each other) was included in this analysis. All quality and stability between-group comparisons were carried out via rank-sum tests.

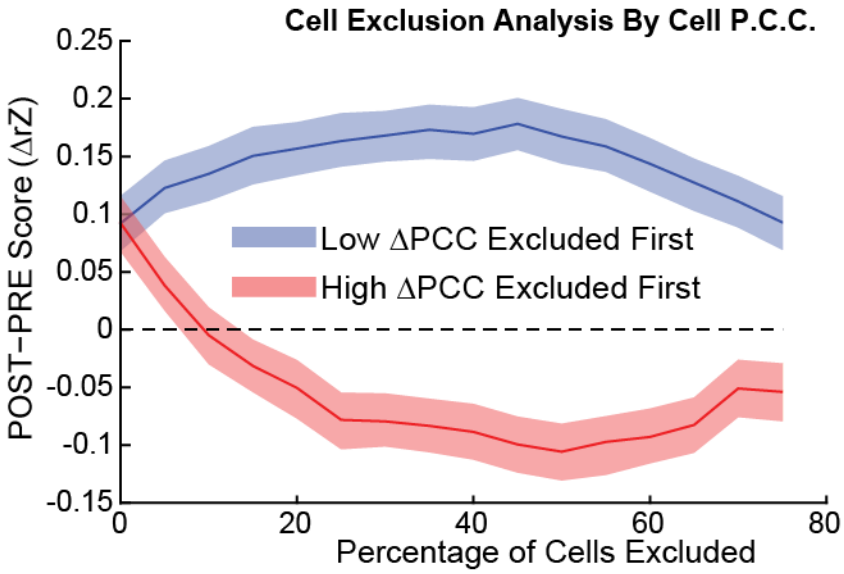

Fig. S12: High ΔPCC cells are necessary and sufficient for PRE to POST increase in sequence content. To assess the contribution of neurons with differing ΔPCC scores to the main ΔReplay (POST rZ – PRE rZ) effect, ΔrZ (y-axis) was calculated from place cell representation matrices in which variable percentages of cells were excluded. In one condition (sorted by PRE - POST PCC score, blue line) an increasing percentage of cells were excluded from the analysis (x-axis) beginning with the ones that showed the lowest ΔPCC values (note that these selections was performed within session, shaded regions show the boot-strapped 95% confidence interval of ΔrZ). Note that even after excluding up to ~75% of 'low' ΔPCC cells, POST epoch sequence content exceeds PRE epoch sequence content, suggesting that these cells are sufficient for the main Δreplay effect. Conversely, in the condition where the cells with high ΔPCC cells were excluded first, after the exclusion of just 10 to 20% of cells PRE epoch sequence content exceeded POST epoch sequence content, suggesting that this 10 to 20% of high ΔPCC cells is necessary for the main Δreplay effect.

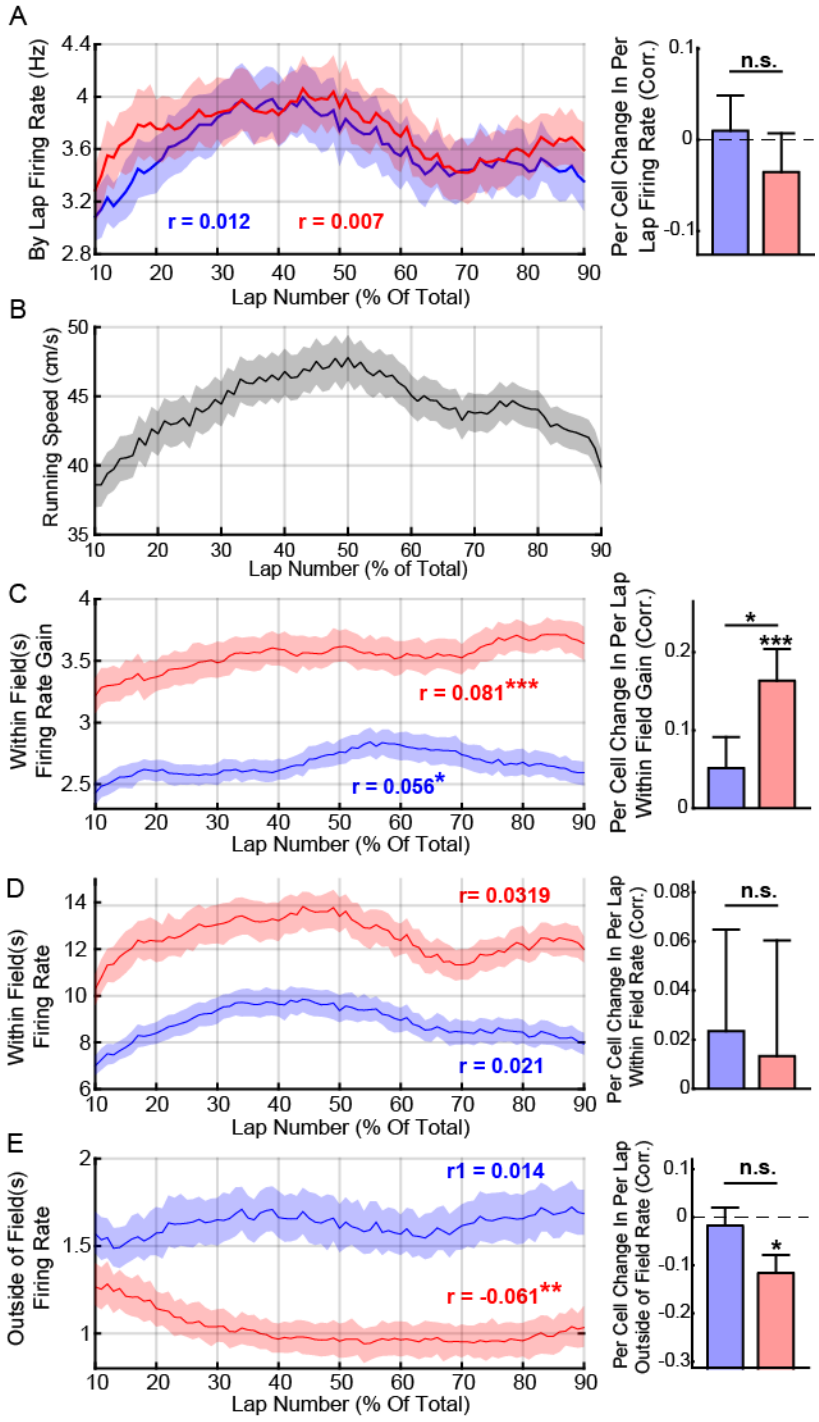

Fig. S13: Within-session firing rate and specificity changes on the maze. (**A**, left panel) Mean firing rate of rigid (blue) and plastic (red) cells is shown as a function of lap number (expressed as a percentage of total number of laps run). The mean (± bootstrapped 95% confidence interval) of each group is shown within a rolling 20% of laps (step-size 1%). The associated Pearson's correlation coefficients were taken across all laps for either all rigid or plastic cells. (**A**, right panel) Per cell quantification: for rigid

and plastic cells, the lap-to-lap firing rate change was computed as the Pearson's correlation between firing rate and lap number. Bar graph shows the mean correlation coefficients ± SE (rank-sum test). These analyses (as well as in Fig. 3B) were restricted to laps in which cells fired at least 5 spikes. (**A**) Neither the populations of rigid or plastic cells show significant changes in over-all firing rate during maze-running. (**B**) However, the overall firing rate (**A**) of both populations closely tracks the variability in running speed across the RUN epoch (only epochs in which the animal was running at > 5 cm/s were included in these analyses). (**C**) In contrast, the by-lap place field gain in firing rate (the ratio of the within place-field(s) rate to overall lap rate) showed a markedly greater increase for plastic cells, which was evident both at the population (**C**, left panel) and individual cell (**C**, right panel) analyses (within cell class: Sign-Rank test across cells' Pearson's correlation coefficients, between cell-class comparison: Rank-Sum test). (**D**) Notably, neither cell group showed a significant increase in within-field firing rate over the course of maze running. (**E**) Conversely, a significant decrease was observed in plastic cells', but not rigid cells', outside of field firing rates. Consequently, we conclude that the observed increase in plastic cells' place specificity was driven primarily by a decreases in their non-place-field specific firing.

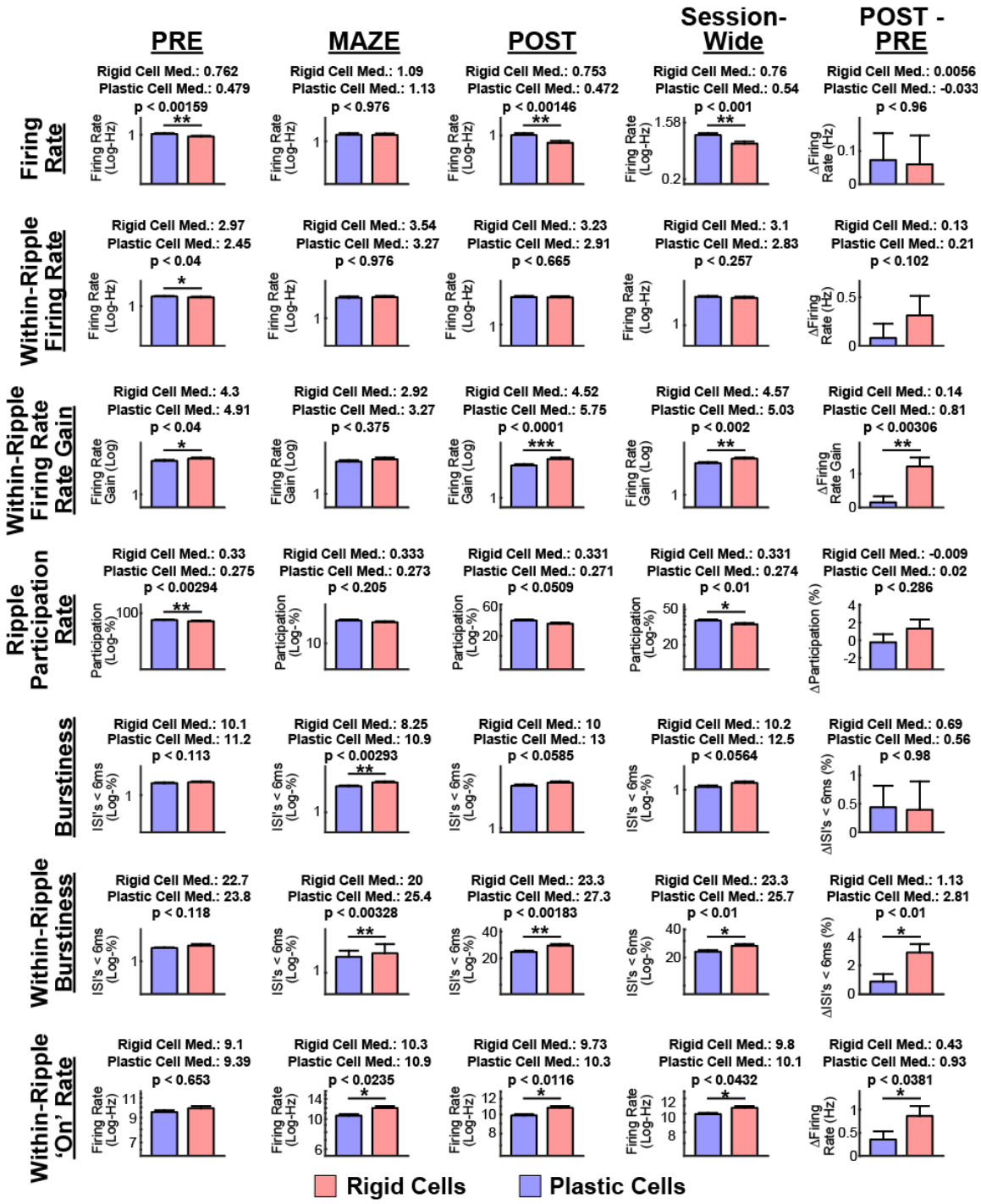

Fig. S14: Excitability characteristics of rigid and plastic cells. The firing patterns of rigid (blue) and plastic (red) cells were characterized using several measures relating to cell excitability during off-line epochs.

1) Firing rate - the number of spikes emitted per second during offline states (quite immobility and NREM sleep).
2) Within-Ripple Firing Rate - the firing rate within concatenated ripple events.

3) Within-Ripple Firing Rate Gain - the within ripple firing rate (2) normalized by the overall firing rate (1)
4) Ripple participation rate - the percentage of ripples a given cell participated in (i.e. fired at least one spike).
5) Burstiness - the percentage of inter-spike-intervals (ISI's) < 6 ms.
6) Within-Ripple Burstiness - the percentage of within-ripple event ISI's < 6 ms.
7) Within-Ripple 'On' Rate - within-ripple firing rate across the subset of ripple events in which the cell fired at least one spike.

These measures are shown for the PRE, MAZE and POST epochs, as well as for their change from PRE to POST. Each panel title shows the median for each distribution as well as the rank-sum p-value for the comparison. Here, as elsewhere, bar graphs plotted in log-scale show the log-mean ± log-SE, while bar graphs plotted in linear scale show the mean ±SE.

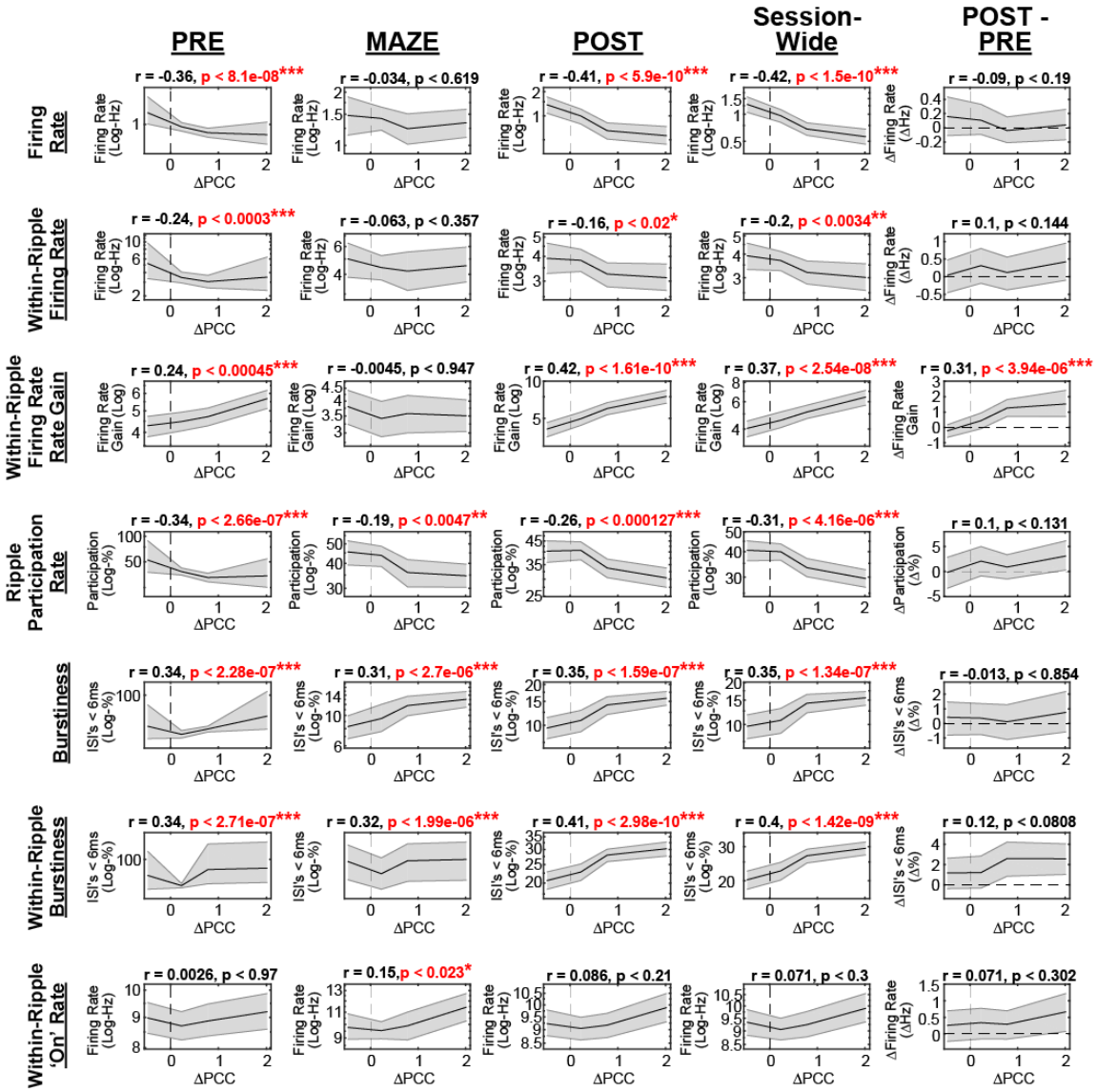

Fig. S15: Excitability characteristics by ΔPCC score. Spearman's correlation coefficients were taken between various measures of excitability (see fig. S12 Legend) and ΔPCC scores for strongly contributing (n = 216) cells (see *Methods* and Fig. 1B). The graphs show the mean ±SE for each of six equally divided subgroups (see fig. S6 legend) – titles show Spearman's correlation coefficient and associated Fisher's Z-test p-values. This analysis is complementary to and independent of that performed using the 'rigid' and 'plastic' cell identification. Since our analysis is best suited for describing those cells that contribute strongly to either the PRE or POST sequence content, we restricted this figure to this subset of cells. However, similar results were obtained when all place cells were considered (data not shown). Note that the relationships obtained using this alternative method which does not rely on within-session matching or cell 'type' classification are in line with our previous findings, suggesting that the reported relationships hold both across and within sessions. Moreover, these results suggest that the 'plastic' and 'rigid' cell properties are continuously distributed within the population.

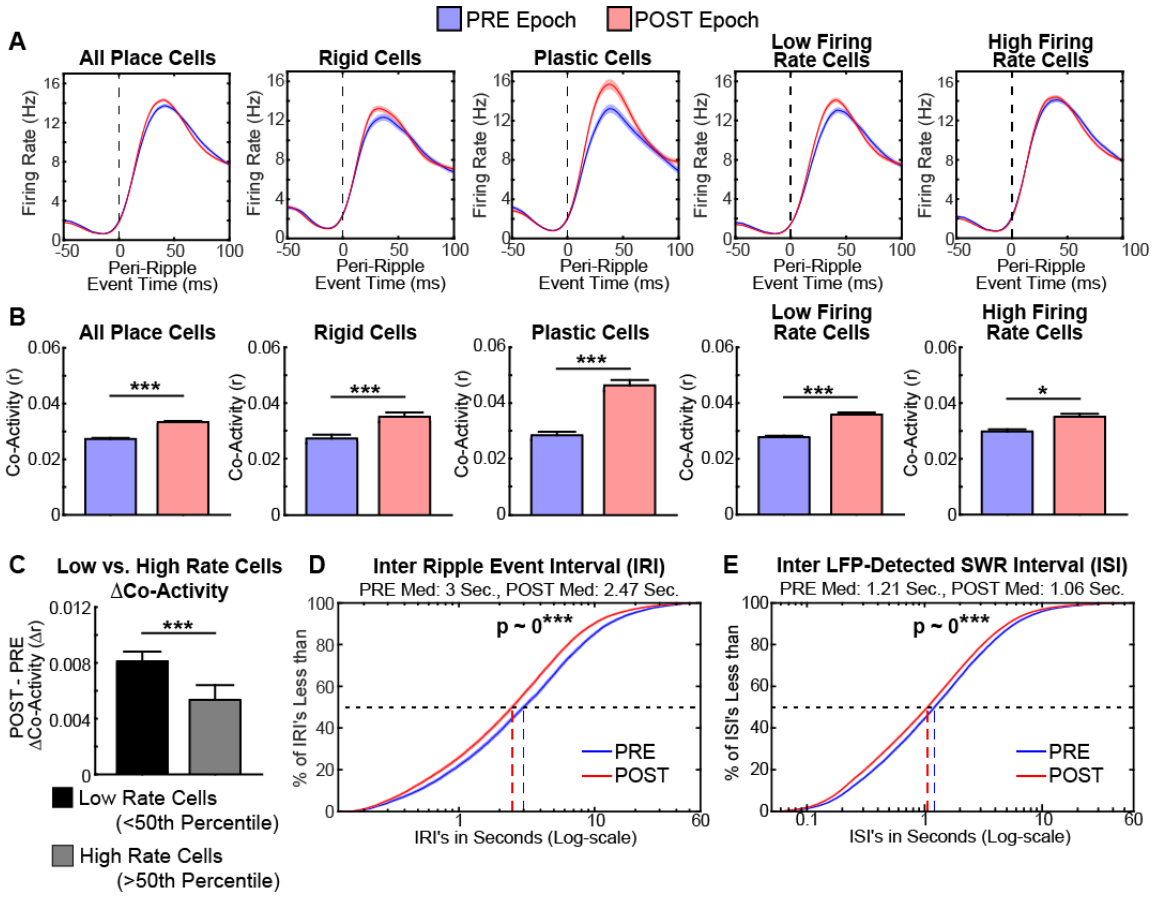

Fig. S16: Synchrony increases from PRE to POST. (**A**) Each panel shows the ripple event-triggered instantaneous firing rates either in the PRE (blue) or POST (red) epochs. Shaded regions show SE of the mean across cells. The PRE to POST increases in ripple-event triggered firing rates seen when all place cells are taken into account (**A**, left panel) are uniquely present in plastic (**A,** third-panel) but not rigid (**A**, second panel) cells. These changes are also more pronounced in low firing rate rather than high firing rate cells (see *Methods* for low and high firing rate classification). Likewise, the PRE to POST increase in pair-wise co-activity observed across all place cells (**B**, left panel) is more robustly observed in the plastic cell population and is more pronounced in low rather than high firing rate cells. Graphs show the mean ± SE for each condition. (**C**) While both low and high firing rate cells increase their synchrony (co-activity) from PRE to POST, the increase in co-activity is greater in low firing rate cells. We note while on the maze low-rate cells also contributed more information per spike (Low Rate median.: 0.91 bits/spike, High Rate med: 0.56 bits/spike, $p < 2.5 \times 10^{-9}$, Rank-Sum test), had a greater within/outside of place field(s) firing ratio (Low Rate med.: 6.38, High Rate med: 3.86, $p < 7.9 \times 10^{-14}$), and had fewer place fields on the maze (Low Rate log-mean: 1.29, High Rate log-mean: 1.59, $p < 3.94 \times 10^{-06}$). In addition, low rate cells tended to show a more pronounced increase in their within-ripple firing rate gain (Low Rate Δripple-gain med.: 0.71, High Rate med.: 0.06, $p < 7.585 \times 10^{-4}$). (**D-E**) Increased synchrony (**B**) in the POST compared to PRE epoch may be attributable to both increases in ripple-triggered spiking (**A**) as well as to an increase in the incidence of ripple events, evident in the incidence of both population synchrony (with associated LFP-detected sharp-wave ripple,

see fig. S4) events used in the rest of the work (**D**) as well as in purely LFP-detected sharp-wave ripple (SWR) events (**E**). The graphs show the cumulative distribution of inter ripple/LFP-SWR event intervals during 'off-line' states – only intervals < 60 sec were considered. P-values show the result of a Rank-Sum test between the two ISI distributions, colored dashed lines show the median of each distribution.

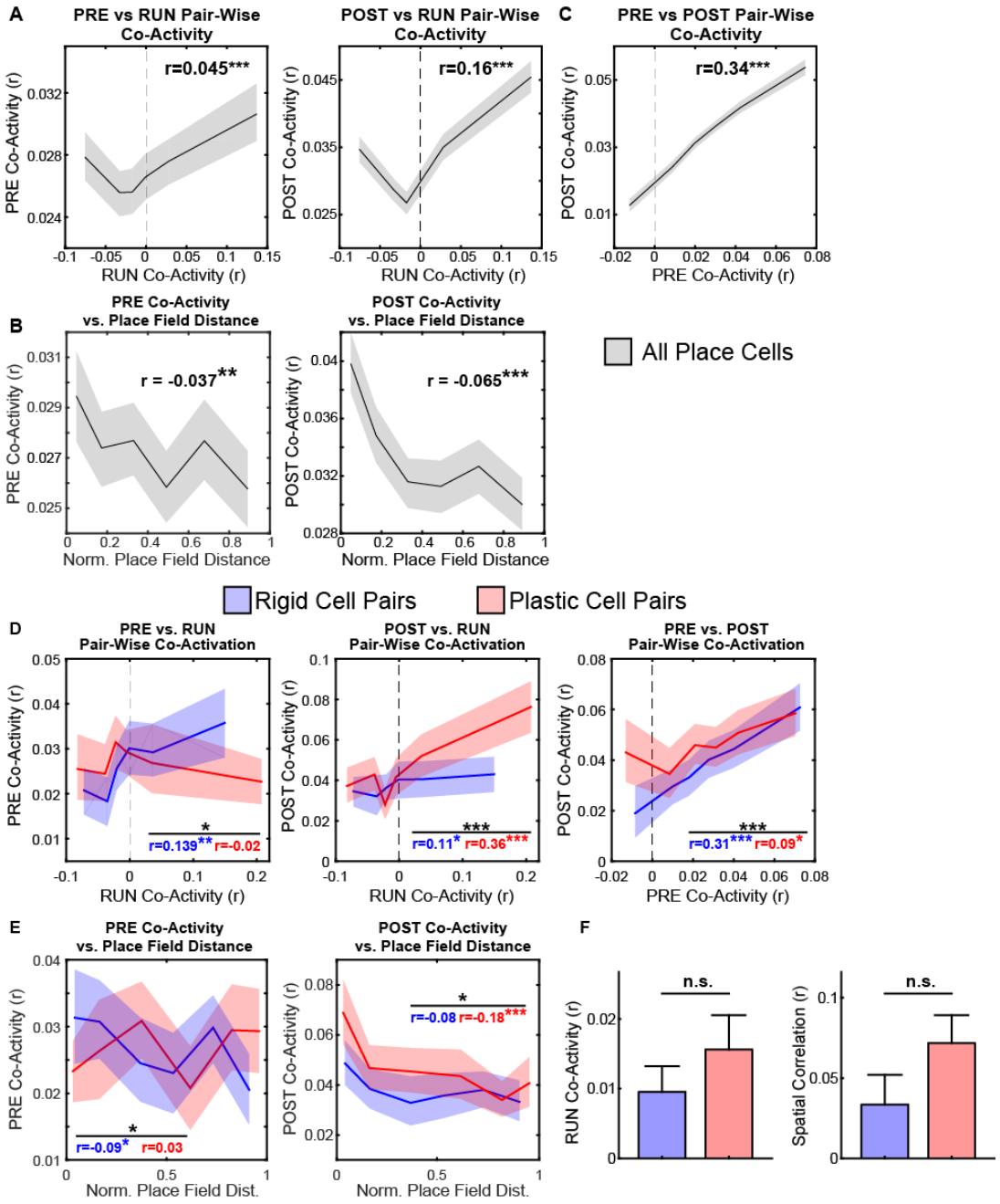

Fig. S17: Pair-wise co-activity patterns display both plastic and rigid components. **(A)** Pair-wise co-activity (Pearson's correlation coefficients between firing rate vectors binned in non-overlapping 100 ms bins) were taken for all place cell pairs which were simultaneously recorded on different shanks either during offline PRE or POST epochs or during active running on the MAZE. Each panel shows the Pearson's correlation coefficient (inset). For each graph the pairs were sub-divided into 6 equal, non-overlapping groups by the condition on the x-ordinate - the graphs show the means ±SE of the corresponding values indicated by the y-ordinate. While co-activity patterns were weakly but significantly preserved from the PRE to the RUN epoch (left panel), the similarity between RUN and POST co-activity patterns (middle panel) was significantly

greater (corr(RUN, POST) - corr(RUN, PRE) = 0.11, $p \approx 0$**,** Fisher's Z-test). However, the similarity between RUN and POST was likewise far exceeded by the similarity between PRE and POST co-activity patterns (corr(PRE, POST) - corr(RUN, POST) = 0.18, $p \approx 0$**,** Fisher's Z-test) suggesting that co-activity patterns during offline states are dominated by non-plastic interactions. **(B)** For each place cell pair, a place field distance was defined as the (2-dimensional) distance between their peak firing rate spatial bins on the maze for each cell and normalized between 0 and 1 by the maximal distance possible on the maze. Note that while place cell's PRE pair-wise co-activity is slightly though significantly predictive of their future place-field distance on the maze (left-panel), this effect is significantly strengthened in the POST epoch (corr(RUN, POST) - corr(RUN, PRE) = -0.035, $p < 0.01$**,** Fisher's Z-test). **(D,** left panel**)** Rigid cell, but not plastic cell, pairs showed preservation of PRE co-activity patterns during the RUN. Conversely, plastic cell pairs showed a significantly higher preservation of co-activity patterns from the RUN to the POST (**D**, middle panel, inset, comparison of correlation coefficients via Fisher Z-test). While both groups showed some degree of stability in their co-activity patterns from the PRE and POST epochs, this effect was significantly more pronounced in rigid cell pairs (**D,** right panel; see also fig. S16 B), suggesting the presence of a more persistent co-activity regime in this latter group. **(E**, left panel**)** Rigid cell, but not plastic cell, PRE pair-wise co-activity was predictive of future place field distance. Conversely, plastic cell pair POST epoch co-activity patterns were significantly more reflective of place field distance (**E,** right panel). (**F**, left panel) rigid and plastic cell pairs did not differ in their pair-wise coactivity strength during running. (**E**) The right panel shows the pair-wise correlation of rigid or plastic cell pairs' firing rate by position vectors (Rank-Sum test between pairs from the two cell classes: $p < 0.24$).

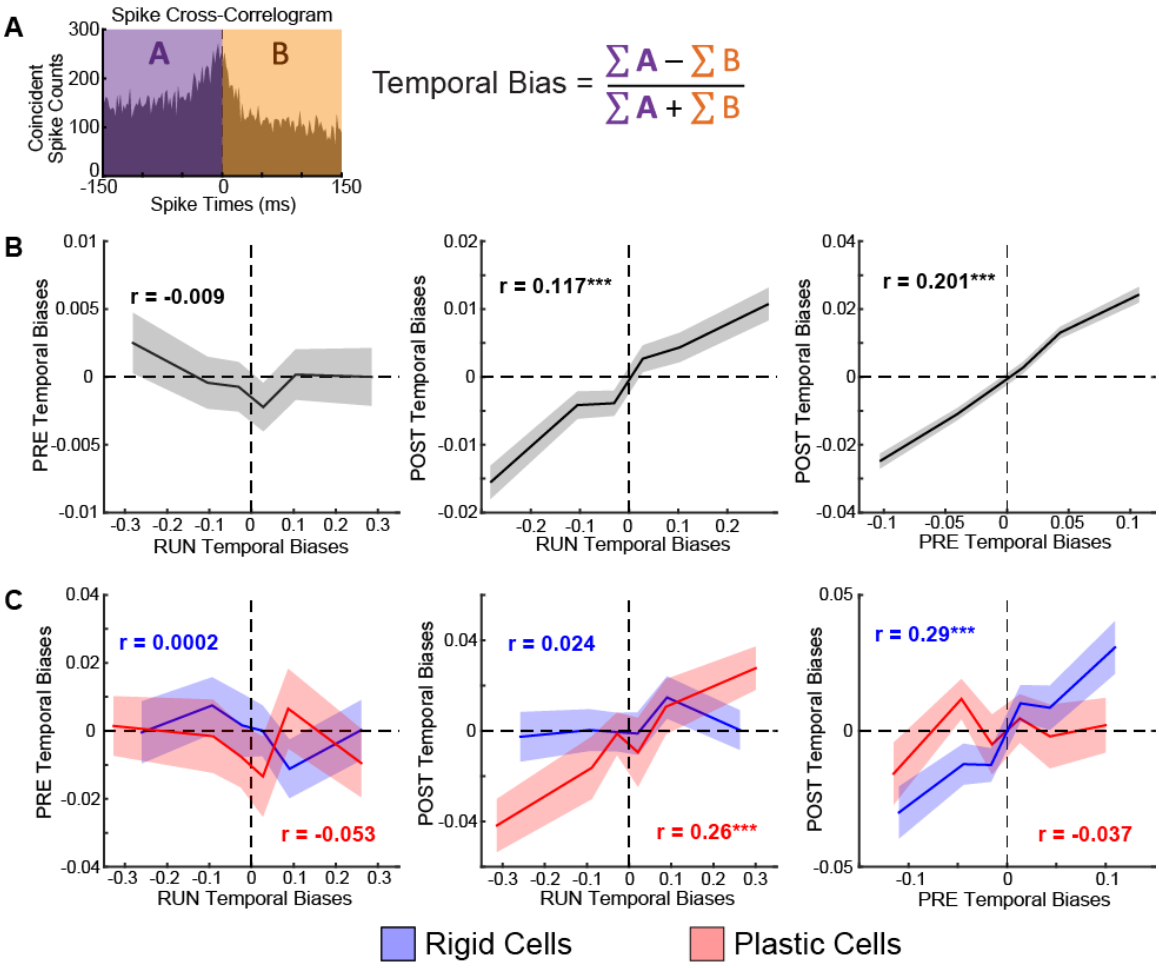

Fig. S18: Pair-wise temporal bias patterns show both plastic and rigid components. (**A**) Sample cross-correlogram illustrating the pair-wise temporal bias measure. Temporal biases were defined as the propensity of one cell to fire before *or* after another cell (within a 150 ms window, see *Methods*). Only pairs of cells recorded on distinct shanks were included in the analysis. Temporal biases were computed from either PRE or POST offline epochs, or during MAZE active running epochs. (**B**) For each of the panels above pairs were divided into 6 equal parts by the temporal bias condition indicated on the x-ordinate, lines show the mean ± SE for these groups in the temporal bias condition shown on the y-ordinate. Insets show the Pearson's correlation coefficient across all pairs. When all place cells are included in the analysis, no similarity is observed between PRE and RUN (left panel) temporal biases. However, temporal biases are strongly preserved from the RUN to POST epochs (middle panel), as well as from the PRE to POST epochs (right). (**C**) Limiting this analysis to rigid (blue) or plastic (red) cell pairs, reveals that the preservation of temporal spiking patterns from PRE to POST and from RUN to POST is attributable to the rigid and plastic cell subpopulations, respectively.

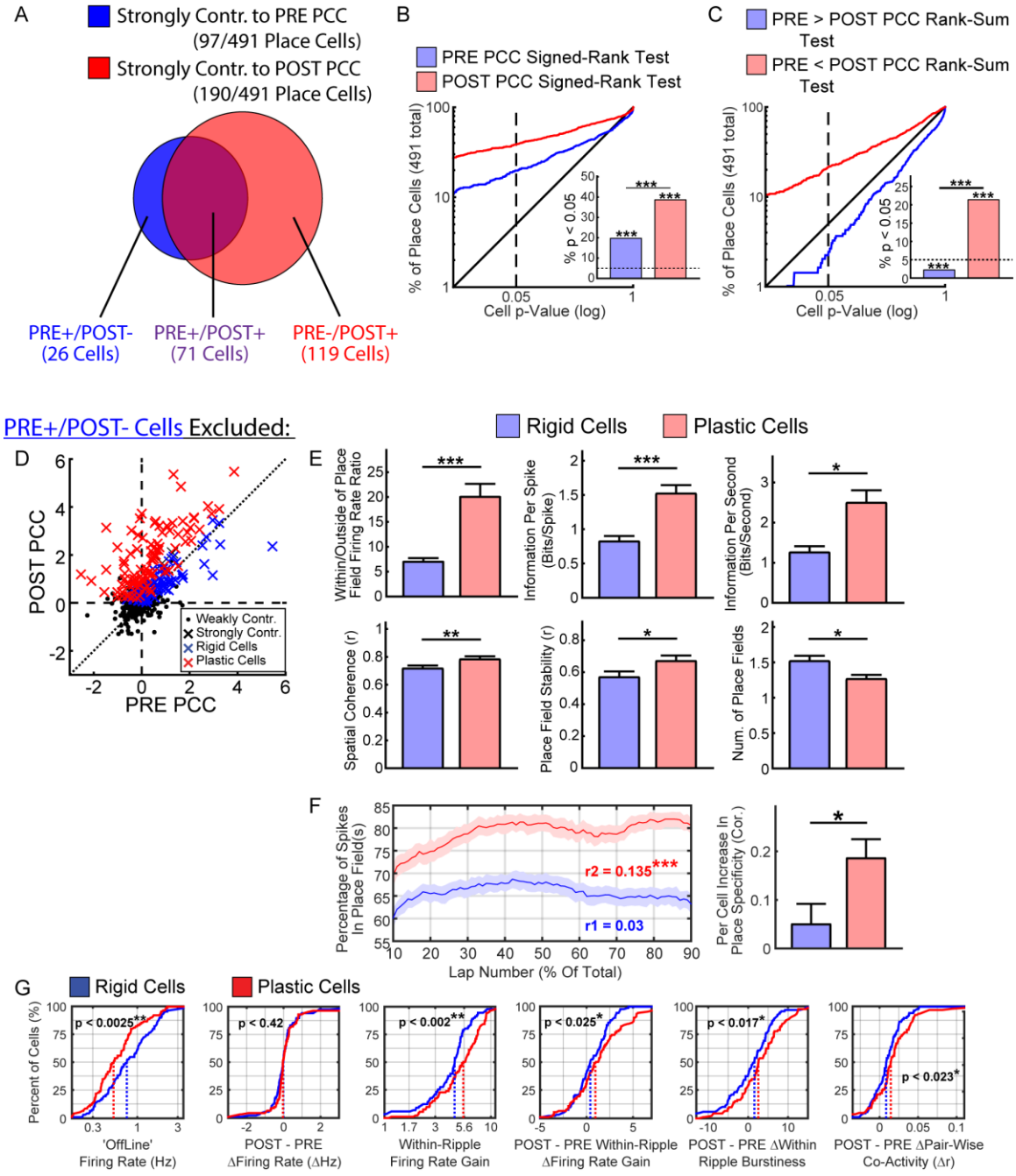

Fig. S19: Rigid cells contribute to both PRE and POST sequence content. (A) The Venn diagram shows the proportion of strongly contributing cells that showed significant PCC scores in PRE-only (blue), POST-only (red), or both (purple) -that the majority (73%) cells showing significant PRE (PRE+) contributions also showed significant POST contributions (POST+). Note that 54% of all putative pyramidal cells were considered to have place fields by running direction. **(B)** Distribution of one-tailed Signed-Rank test p-values across per-event PCC scores in either the PRE (blue) or POST (red) epochs. Those cells significant ($p < 0.05$) for either of these comparisons were taken as strongly contributing to sequence content. **(C)** In order to further probe changes in PRE and POST PCC scores for each cell, one-tailed rank-sum tests were performed for testing the

hypothesis that within-event PCC scores were either higher in the PRE (blue) or POST epochs. 2.2% of cells showed significantly greater PRE compared to POST PCC scores while 21.4% showed higher POST > PRE. Together, these results suggest that those cells contributing PRE 'rigidly' continued contributing to POST. **(D)** In order to test whether our results were consistent with the absence of a true 'PRE-only' signal, we excluded these 26 cells (thereby including only cells that had significant POST PCC scores – A, red and purple area) and repeated our main analyses. This exclusion analysis confirmed that our main findings regarding differences in rigid versus plastic cell spatial coding **(E,** compare to Fig. 3A**)**, changes in spatial coding during the course of maze-running **(F**, compare to Fig. 3B**)** and excitability and synchrony **(G,** compare to Fig. 4A**)** were observed independently of the small PRE-only cell subset.

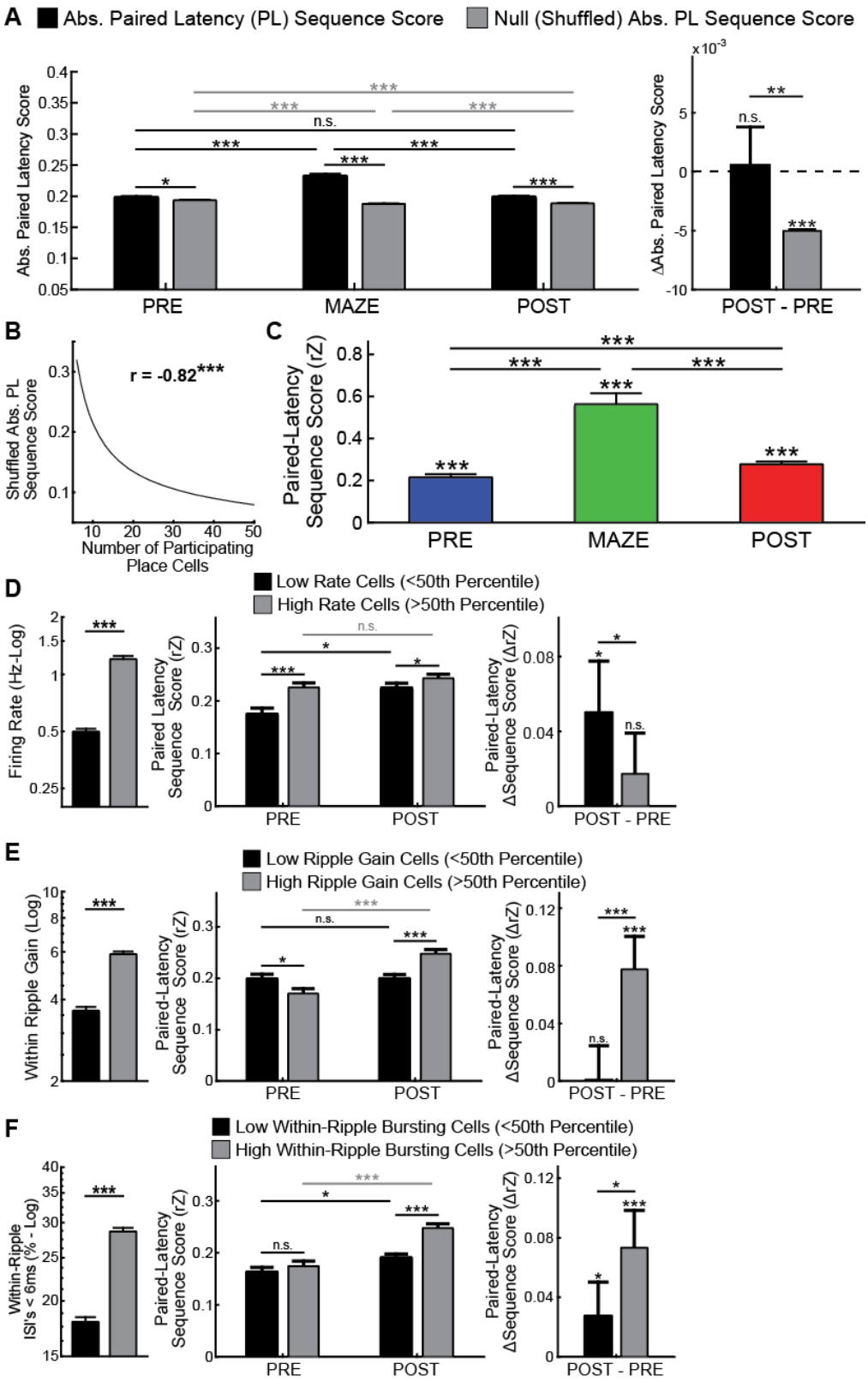

Fig. S20: Paired-Latency (non-Bayesian) analysis of PRE and POST sequences. To test the findings obtained using the Bayesian weighted-correlation sequence scoring

method, a parallel analysis was performed using a non-Bayesian 'Paired-Latency' (PL) template matching method. Importantly, and in distinction to the Bayesian method, for each place cell this method only takes into account the location (spatial bin) displaying the peak firing rate during maze running, and the temporal center of mass of spiking during a given offline ripple event (displayed as diamonds in figure 2C). In addition, this method excluded the possible influence of within-shank interactions. For this analysis (in contrast to the Bayesian weighted correlation analysis), the null distribution was determined by shuffling cell identities of the place field peaks. (**A**) While the PL method revealed that the observed sequence scores were greater than their null counterparts in the PRE, MAZE and POST epochs, PRE to POST increases in sequence content were not evident using this analysis. However, this was accounted for by the fact that in the PL analysis (and contrary to the Bayesian weighted correlation method, see fig. S5) the sequence scores associated with the null distribution dropped sharply from the PRE to POST epochs. (**B**) The observed decrease in abs. *PL(null)*is predicted by the increase in the number of participating cells from PRE to POST (fig. S5F), and the strong negative relationship between number of participants and expected shuffled abs. PL value (panel shows, mean ±SE for each of 18 log-spaced bins). Note that since not all cells with place fields in one running direction will also have place fields in the opposite running direction, the underlying *null* statistics of events may differ between directions of the RUN-template. Therefore, 'bimodal' shuffling procedures in which the greater *null* value is taken across directions (*14*) will tend to compare abs. *r(observed)* values against abs. *r(null)* values drawn from null distributions with means higher than those of the true null distributions of the events themselves. For this reason we independently compared the results of each running direction to its null distribution. (**C**) Once the null distribution is taken into account by computing the PL distribution's rZ scores, PL estimated sequence content is qualitatively similar in PRE, MAZE and POST as those observed using the Bayesian weighted correlation method (annotations same as in Fig. 1C). Likewise, using this separate method the main Δreplay (POST - PRE) effect was confirmed to be attributable to low-firing rate (**D**) high-ripple gain (**E**) high-ripple bursting (**F**) cells, while high-firing rate, low-ripple gain, low ripple bursting, cells were similarly confirmed to be the more associated with PRE sequence content.

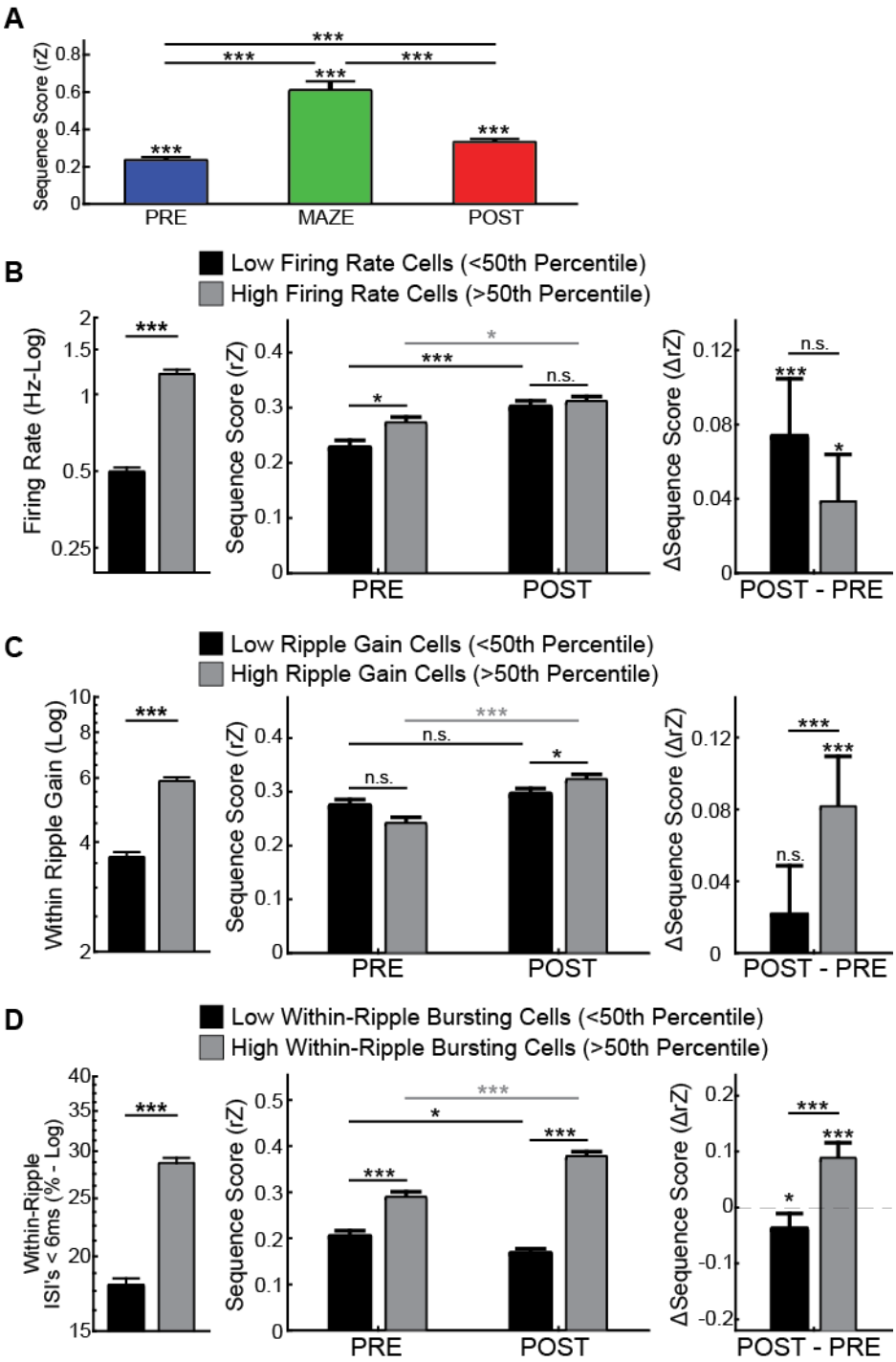

Fig. S21: Burst-controlled analysis of sequence content. Since the Bayesian decoder employed in this work assumes a Poisson distribution of spiking (*36*) and this assumption may be violated by burst events, a 'decimated' control data set was constructed in which only the first spike of each within-ripple burst (defined as any series of spikes with ISI's < 6ms) was included. The Bayesian weighted correlation analysis was performed on this decimated data set. (**A**) The qualitative relationship of decoded sequence content is preserved after burst decimation. This downsampled data set was divided into low and

high ‘offline’ firing rate (**B**), within-ripple gain (**C**), and within-ripple bursting cells (**D**), as defined from the original (none-decimated) data set. Note that the left panels in **B-D** show the values of each of the sub-distributions in the non-decimated data set (in the decimated data set the within-ripple bursting was 0% for all cells). In this down sampled data set replay was also found to be associated with low rate, high ripple gain, high ripple bursting cells, while high rate, low ripple gain, low ripple bursting cells were more associated with PRE sequence content.

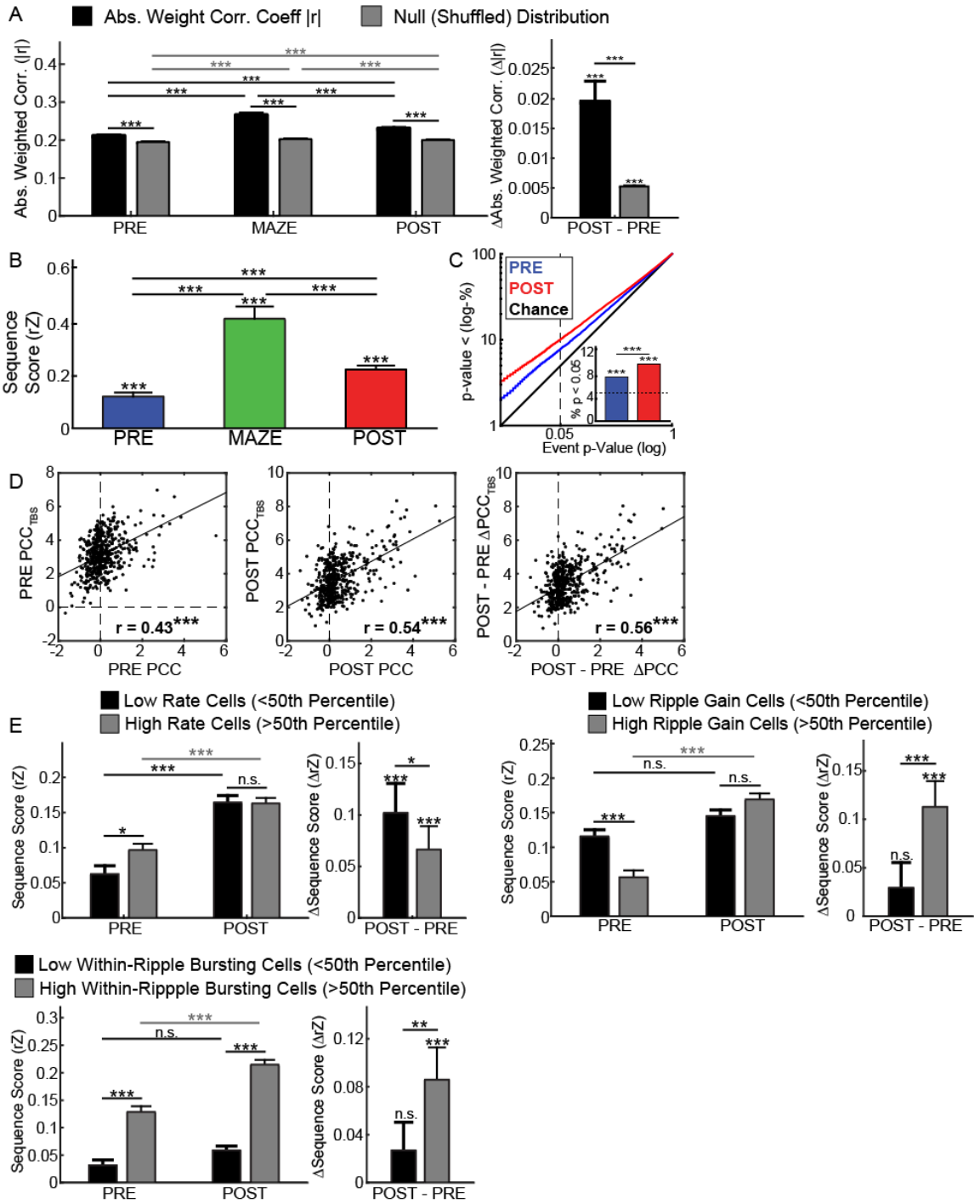

Fig. S22. Column Shuffle Results. Since differing shuffling techniques make differing assumptions and may therefore be susceptible to differing biases, our main results were tested using an alternative and complementary shuffling technique in which the 20ms time bins within each ripple-event were permuted (time-bin shuffle, TBS). Note that in this shuffling approach place field templates were maintained as observed. When compared to the place-field circular shuffling technique the TBS method yielded similar results for absolute weighted correlations **(A)**, sequence scores (rZ, **B**) and Monte-Carlo

significance testing **(C,** compare to Fig. 1C and fig. S5 B, C**).** An alternative PCC estimation method was developed in which each cell's firing rate-by-time bin vectors were randomly permuted within each event (PCC_{TBS} see *Methods*). **(D)** PCC_{TBS} estimates of each cell's contribution to sequence content were highly correlated with those obtained by our primary PCC method in the PRE, POST as well as in the PRE to POST change. **(E)** Using the TBS method low-firing rate, high within-ripple firing rate gain, high within-ripple bursting cells were confirmed to display the strongest increases in PRE to POST sequence content.

References

1. L. N. John O'Keefe, *The Hippocampus as a Cognitive Map* (Oxford Univ. Press, Oxford, 1978).

2. T. J. Davidson, F. Kloosterman, M. A. Wilson, Hippocampal replay of extended experience. *Neuron* **63**, 497–507 (2009). Medline doi:10.1016/j.neuron.2009.07.027

3. K. Diba, G. Buzsáki, Forward and reverse hippocampal place-cell sequences during ripples. *Nat. Neurosci.* **10**, 1241–1242 (2007). Medline doi:10.1038/nn1961

4. D. J. Foster, M. A. Wilson, Reverse replay of behavioural sequences in hippocampal place cells during the awake state. *Nature* **440**, 680–683 (2006). Medline doi:10.1038/nature04587

5. B. E. Pfeiffer, D. J. Foster, Hippocampal place-cell sequences depict future paths to remembered goals. *Nature* **497**, 74–79 (2013). Medline doi:10.1038/nature12112

6. D. Dupret, J. O'Neill, B. Pleydell-Bouverie, J. Csicsvari, The reorganization and reactivation of hippocampal maps predict spatial memory performance. *Nat. Neurosci.* **13**, 995–1002 (2010). Medline doi:10.1038/nn.2599

7. G. Girardeau, K. Benchenane, S. I. Wiener, G. Buzsáki, M. B. Zugaro, Selective suppression of hippocampal ripples impairs spatial memory. *Nat. Neurosci.* **12**, 1222–1223 (2009). Medline doi:10.1038/nn.2384

8. H. S. Kudrimoti, C. A. Barnes, B. L. McNaughton, Reactivation of hippocampal cell assemblies: Effects of behavioral state, experience, and EEG dynamics. *J. Neurosci.* **19**, 4090–4101 (1999). Medline

9. A. K. Lee, M. A. Wilson, Memory of sequential experience in the hippocampus during slow wave sleep. *Neuron* **36**, 1183–1194 (2002). Medline doi:10.1016/S0896-6273(02)01096-6

10. M. A. Wilson, B. L. McNaughton, Reactivation of hippocampal ensemble memories during sleep. *Science* **265**, 676–679 (1994). Medline doi:10.1126/science.8036517

11. G. Buzsáki, Two-stage model of memory trace formation: A role for "noisy" brain states. *Neuroscience* **31**, 551–570 (1989). Medline doi:10.1016/0306-4522(89)90423-5

12. M. E. Hasselmo, Neuromodulation: Acetylcholine and memory consolidation. *Trends Cogn. Sci.* **3**, 351–359 (1999). Medline doi:10.1016/S1364-6613(99)01365-0

13. G. Buzsáki, Hippocampal sharp wave-ripple: A cognitive biomarker for episodic memory and planning. *Hippocampus* **25**, 1073–1188 (2015). Medline doi:10.1002/hipo.22488

14. D. Silva, T. Feng, D. J. Foster, Trajectory events across hippocampal place cells require previous experience. *Nat. Neurosci.* **18**, 1772–1779 (2015). Medline doi:10.1038/nn.4151

15. W. Gerstner, W. M. Kistler, R. Naud, L. Paninski, *Neuronal Dynamics: From Single Neurons to Networks and Models of Cognition* (Cambridge Univ. Press, 2014).

16. K. Mizuseki, G. Buzsáki, Preconfigured, skewed distribution of firing rates in the hippocampus and entorhinal cortex. *Cell Reports* **4**, 1010–1021 (2013). Medline doi:10.1016/j.celrep.2013.07.039

17. D. Panas, H. Amin, A. Maccione, O. Muthmann, M. van Rossum, L. Berdondini, M. H. Hennig, Sloppiness in spontaneously active neuronal networks. *J. Neurosci.* **35**, 8480–8492 (2015). Medline doi:10.1523/JNEUROSCI.4421-14.2015

18. G. Dragoi, S. Tonegawa, Preplay of future place cell sequences by hippocampal cellular assemblies. *Nature* **469**, 397–401 (2011). Medline doi:10.1038/nature09633

19. G. Dragoi, S. Tonegawa, Distinct preplay of multiple novel spatial experiences in the rat. *Proc. Natl. Acad. Sci. U.S.A.* **110**, 9100–9105 (2013). Medline doi:10.1073/pnas.1306031110

20. H. F. Ólafsdóttir, C. Barry, A. B. Saleem, D. Hassabis, H. J. Spiers, Hippocampal place cells construct reward related sequences through unexplored space. *eLife* **4**, e06063 (2015). Medline doi:10.7554/eLife.06063

21. Materials and methods are available as supplementary materials on *Science* Online.

22. G. Dragoi, K. D. Harris, G. Buzsáki, Place representation within hippocampal networks is modified by long-term potentiation. *Neuron* **39**, 843–853 (2003). Medline doi:10.1016/S0896-6273(03)00465-3

23. K. C. Bittner, C. Grienberger, S. P. Vaidya, A. D. Milstein, J. J. Macklin, J. Suh, S. Tonegawa, J. C. Magee, Conjunctive input processing drives feature selectivity in hippocampal CA1 neurons. *Nat. Neurosci.* **18**, 1133–1142 (2015). Medline doi:10.1038/nn.4062

24. S. Cheng, L. M. Frank, New experiences enhance coordinated neural activity in the hippocampus. *Neuron* **57**, 303–313 (2008). Medline doi:10.1016/j.neuron.2007.11.035

25. P. D. Rich, H.-P. Liaw, A. K. Lee, Large environments reveal the statistical structure governing hippocampal representations. *Science* **345**, 814–817 (2014). Medline doi:10.1126/science.1255635

26. S. Ciocchi, J. Passecker, H. Malagon-Vina, N. Mikus, T. Klausberger, Selective information routing by ventral hippocampal CA1 projection neurons. *Science* **348**, 560–563 (2015). Medline doi:10.1126/science.aaa3245

27. G. Buzsáki, Our skewed sense of space. *Science* **347**, 612–613 (2015). Medline doi:10.1126/science.aaa6505

28. M. Vandecasteele, S. M, S. Royer, M. Belluscio, A. Berényi, K. Diba, S. Fujisawa, A. Grosmark, D. Mao, K. Mizuseki, J. Patel, E. Stark, D. Sullivan, B. Watson, G. Buzsáki, Large-scale recording of neurons by movable silicon probes in behaving rodents. *J. Vis. Exp.* **2012**, e3568 (2012). Medline

29. K. D. Harris, D. A. Henze, J. Csicsvari, H. Hirase, G. Buzsáki, Accuracy of tetrode spike separation as determined by simultaneous intracellular and extracellular measurements. *J. Neurophysiol.* **84**, 401–414 (2000). Medline

30. J. O'Neill, T. J. Senior, K. Allen, J. R. Huxter, J. Csicsvari, Reactivation of experience-dependent cell assembly patterns in the hippocampus. *Nat. Neurosci.* **11**, 209–215 (2008). Medline doi:10.1038/nn2037

31. A. D. Grosmark, K. Mizuseki, E. Pastalkova, K. Diba, G. Buzsáki, REM sleep reorganizes hippocampal excitability. *Neuron* **75**, 1001–1007 (2012). Medline doi:10.1016/j.neuron.2012.08.015

32. K. Mizuseki, S. Royer, K. Diba, G. Buzsáki, Activity dynamics and behavioral correlates of CA3 and CA1 hippocampal pyramidal neurons. *Hippocampus* **22**, 1659–1680 (2012). Medline doi:10.1002/hipo.22002

33. X. Wu, D. J. Foster, Hippocampal replay captures the unique topological structure of a novel environment. *J. Neurosci.* **34**, 6459–6469 (2014). Medline doi:10.1523/JNEUROSCI.3414-13.2014

34. W. E. Skaggs, B. L. McNaughton, Replay of neuronal firing sequences in rat hippocampus during sleep following spatial experience. *Science* **271**, 1870–1873 (1996). Medline doi:10.1126/science.271.5257.1870

35. G. Buzsáki, J. Csicsvari, G. Dragoi, K. Harris, D. Henze, H. Hirase, Homeostatic maintenance of neuronal excitability by burst discharges in vivo. *Cereb. Cortex* **12**, 893–899 (2002). Medline doi:10.1093/cercor/12.9.893

36. Z. Chen, An overview of Bayesian methods for neural spike train analysis. *Comput. Intell. Neurosci.* **2013**, 251905 (2013). Medline doi:10.1155/2013/251905